Am J Nucl Med Mol Imaging 2026;16(2):90-99
www.ajnmmi.us /ISSN:2160-8407/ajnmmi0171247

*Original Article*

# Development and evaluation of a novel deuterated fluorine-18 PET tracer for MAO-B imaging

Chongyi Huang, Huiyi Wei, Haige Yi, Guocong Li, Weiyuan Lin, Taoqian Zhao, Yinlong Li, Steven H Liang, Hao Xu, Lu Wang

*State Key Laboratory of Bioactive Molecules and Druggability Assessment, Guangdong Basic Research Center of Excellence for Natural Bioactive Molecules and Discovery of Innovative Drugs, Department of Nuclear Medicine, The First Affiliated Hospital, Jinan, China*

Received January 5, 2026; Accepted February 13, 2026; Epub April 15, 2026; Published April 30, 2026

**Abstract:** Monoamine oxidase B (MAO-B) is a key astrocytic biomarker implicated in neuro-inflammation and neurodegenerative diseases. This study reports the development and evaluation of novel fluorine-18 ($^{18}$F) PET radiotracers for selective MAO-B imaging by exploiting deuteration strategies to address metabolic instability of existing probes. A literature compound [$^{18}$F]GEH200449 ([$^{18}$F]4) was synthesized through redesigned labeling precursor, and its deuterated analogue, [$^{18}$F]4-$D_2$, was prepared to improve metabolic stability. Systematic evaluation using PET imaging, radiometabolite analysis, and autoradiography was performed. While both tracers demonstrated favorable blood-brain barrier penetration, they didn't exhibit region-specific binding consistent with MAO-B distribution in vivo. Furthermore, [$^{18}$F]4 underwent substantial metabolic degradation in both central and peripheral compartments, and deuteration failed to provide significant stabilization in [$^{18}$F]4-$D_2$. Autoradiography further revealed non-selective binding of [$^{18}$F]4-$D_2$ to both MAO isoforms. Overall, the translational potential of [$^{18}$F]4 and [$^{18}$F]4-$D_2$ remains limited by poor metabolic stability and insufficient target selectivity. Future tracer design should focus on pharmacophore optimization to achieve reliable and selective MAO-B PET imaging.

**Keywords:** Monoamine oxidase B, PET, Fluorine-18, deuterium, radiometabolites

## Introduction

Monoamine oxidase (MAO), a flavin-dependent enzyme primarily localized within glial cells [1], plays a critical role in the oxidative deamination of monoamine neurotransmitters, including dopamine, serotonin, adrenaline, and noradrenaline, thereby maintaining neurotransmitter homeostasis in the central nervous system (CNS) [2]. The enzyme exists in two distinct isoforms, MAO-A and MAO-B, which are classified according to their substrate preference, inhibitor sensitivity, and pharmacological properties [3]. Both isoforms have been extensively studied in the pathophysiology and treatment of neurological and psychiatric disorders such as major depressive disorder, Alzheimer's disease, anxiety-related conditions, and Parkinson's disease [4-7]. In the primate and human CNS, MAO-B predominates over MAO-A and catalyzes the oxidative deamination of dopamine to form dihydroxyphenylacetic acid (DOPAC), which is subsequently metabolized to homovanillic acid (HVA). MAO-B expression increases markedly during the course of normal aging as well as in neurodegenerative pathologies [6, 8]. This increase has been mechanistically associated with reactive gliosis, a process characterized by astrocytic proliferation and hypertrophy in response to neuronal injury [9, 10]. Activated astrocytes exhibit pronounced upregulation of MAO-B on their outer mitochondrial membranes, which has been implicated in the initiation and amplification of neuroinflammatory cascades [11, 12]. These properties have positioned MAO-B as a promising biomarker for the non-invasive imaging of astrocyte activation [13], and as a therapeutic target in Parkinson's disease, depression, and Alzheimer's disease [3, 14-16].

Positron emission tomography (PET) is a non-invasive, highly sensitive molecular imaging technique in nuclear medicine that enables quantitative visualization of physiological and biochemical processes in vivo through radiotracer-based detection [17]. Given its ability to interrogate molecular targets in the living brain, PET has become an indispensable tool in neuroimaging. Selective PET imaging of MAO-B has therefore been the focus of extensive tracer development efforts. Fang and colleagues [18] categorized MAO-B PET ligands into three mechanistic classes: irreversible binders, reversible binders, and metabolic trapping radioligands. Clinical investigations have largely focused on irreversible ligands such as L-[$^{11}$C]deprenyl and its deuterated analog [$^{11}$C]-L-deprenyl-$D_2$, as well as the reversible ligand [$^{11}$C]SL25.1188, for the quantification of cerebral MAO-B in humans [19-21]. Despite their utility, the widespread clinical application of carbon-11 labeled tracers is limited by the isotope's short half-life (20.4 minutes), which requires on-site cyclotron production and restricts their broader dissemination. This challenge stimulated the development of fluorine-18 labeled alternatives, which offer a longer half-life (109.8 minutes), simplified radiochemistry logistics, and broader clinical accessibility.

In this context, a series of fluorine-18 labeled MAO-B probes were reported, including [$^{18}$F]fluororasagiline [22],


https://doi.org/10.62347/CRAH2142

its deuterated analog [$^{18}$F]fluororasagiline-$D_2$ [23], and [$^{18}$F]GEH200449 ([$^{18}$F]4) [24]. In vitro autoradiography studies in healthy human brain tissue and PET studies in monkeys demonstrated selective binding of these tracers to MAO-B-rich regions such as the striatum, supporting their potential as imaging agents. However, tracer interpretation was complicated by the formation of radiometabolites capable of crossing the blood-brain barrier (BBB), which introduced confounding nonspecific signals. To mitigate this, a deuteration strategy was employed in the design of L-[$^{18}$F]Deprenyl to improve metabolic stability, though concerns persisted regarding the formation of brain-penetrant metabolites, such as [$^{18}$F]fluorometamphetamine-$D_2$, which could undermine tracer quantification [25]. Among the fluorine-18 based candidates, [$^{18}$F]4 is particularly promising, as it demonstrated high binding specificity for MAO-B and minimal nonspecific binding in human brain autoradiography. Subsequent non-human primates (NHPs) PET studies further supported its suitability as a reversible MAO-B radioligand, advancing it as a strong candidate for translational MAO-B imaging [26]. Building on these findings, the present study sought to conduct a comprehensive in vivo evaluation of [$^{18}$F]4 and its deuterated analog before translating into human studies. Pharmacokinetic profiles of [$^{18}$F]4 and [$^{18}$F]4-$D_2$ were systematically examined in rodents, and the results of these investigations are presented herein.

## Material and methods

*Radiolabeling*

[$^{18}$F]4 and [$^{18}$F]4-$D_2$ were synthesized under identical radiolabeling conditions using a TRACERlab® FX2N synthesizer module. Radiosynthesis commenced with the production of [$^{18}$F]fluoride via proton bombardment (10.0 MeV, Minitrace™ Qilin cyclotron; GE Healthcare, USA) of > 98% enriched $H_2{}^{18}O$ (TAIYO NIPPON SANSO Corporation, Tokyo, Japan). The [$^{18}$F]fluoride was trapped on a pre-conditioned Sep-Pak® QMA Plus Light cartridge and eluted into a 4 mL reaction vial containing a solution of $K_2CO_3$ (6.0 mg) and K2.2.2 (20.0 mg) in $CH_3CN/H_2O$ (7:3 v/v, 1.0 mL). The eluate was dried under nitrogen at 110°C for 8 min. The precursor (2.0 mg), dissolved in anhydrous $CH_3CN$ (1.0 mL), was then added to the reaction vial, and radiolabeling proceeded at 85°C for 5 min. The reaction mixture was quenched, diluted with water (2.0 mL), and purified by semi-preparative HPLC (CAPCELL PAK C18 UG80, 5 μm, 10 × 250 mm, Osaka Soda Co., Ltd.; mobile phase: $CH_3CN/H_2O$ (7:13 v/v) containing 0.1% triethylamine; flow rate: 3 mL/min). The radioactive ligand eluted at approximately 21 min, after which the product fraction was collected, diluted with sterile water (80 mL), and loaded onto a Sep-Pak® Light C18 cartridge. The cartridge was rinsed with sterile water (10 mL), and [$^{18}$F]4/[$^{18}$F]4-$D_2$ was eluted with absolute ethanol (1 mL). The ethanolic eluate was diluted with sterile saline (9 mL) to yield the final injectable solution. Radiochemical and chemical purity were assessed by analytical HPLC (GL Science WondaSil C18, 5 μm, 150 × 4.6 mm; UV detection: 254 nm; mobile phase: $CH_3CN/H_2O$ (7:13 v/v); flow rate: 1 mL/min). Identity was confirmed by co-injection (20 μL sample) with the corresponding non-radiolabeled reference standard.

*Radiometabolite analysis*

Sprague-Dawley (SD) rats (n = 3 per time point) were anesthetized with isoflurane and intravenously administered [$^{18}$F]4/[$^{18}$F]4-$D_2$ via the tail vein. Animals were sacrificed at 20 or 60 minutes post-injection. Blood and brain tissues were rapidly harvested. Blood samples were centrifuged (6,000 rpm, 4°C, 5 min) to obtain plasma. A 0.5 mL aliquot of plasma was mixed with 0.5 mL of acetonitrile, vortexed for 30 s, and centrifuged (14,000 rpm, 4°C, 3 min). Brain samples were homogenized in 1 mL of ice-cold acetonitrile and centrifuged under the same conditions. Supernatants from plasma and brain homogenates were diluted with water (1:1 v/v), and 50 μL of non-radiolabeled reference standard (1 mg/mL) was added to each sample. Radiometabolites were analyzed by semi-preparative HPLC (CAPCELL PAK C18 UG80, 5 μm, 10 × 250 mm; mobile phase: $CH_3CN/H_2O$ (9:11 v/v) containing 0.1% triethylamine; flow rate: 4 mL/min). Fractions were collected every 30 s over 15 min, and radioactivity was quantified using a 2480 Wizard automatic gamma counter (PerkinElmer, USA). All values were decay-corrected, and radiochromatograms were reconstructed. The percentage of intact tracer was calculated as the ratio of radioactivity in parent compound fractions to total recovered radioactivity, multiplied by 100.

*In vitro autoradiography*

Transverse brain sections (20 μm) from male Sprague-Dawley rats (7-8 weeks old, 220-250 g) were prepared and stored at -80°C. Sections were thawed, air-dried under a cold stream, and pre-incubated for 10 min in assay buffer (50 mM Tris-HCl, pH 7.4, containing 120 mM NaCl, 5 mM KCl, 2 mM $CaCl_2$, and 0.1% bovine serum albumin). For baseline binding, sections were incubated with [$^{18}$F]4-$D_2$ (90 μCi in 180 mL assay buffer) for 90 min at room temperature. After incubation, sections were washed twice in ice-cold assay buffer (10 min each), rinsed briefly in ice-cold deionized water, and dried. Dried sections were exposed to phosphorimaging plates (Amersham Typhoon; Cytiva, USA) for 30 min, and autoradiograms were acquired using a Bio-Imaging Analyzer System (Multi Gauge Version 2.3; FUJIFILM). Photostimulated luminescence values were quantified in predefined brain regions. For blocking studies, adjacent sections were co-incubated with [$^{18}$F]4-$D_2$ and either L-deprenyl (10 μM) or pirlindole (10 μM), followed by the same washing and detection procedures.

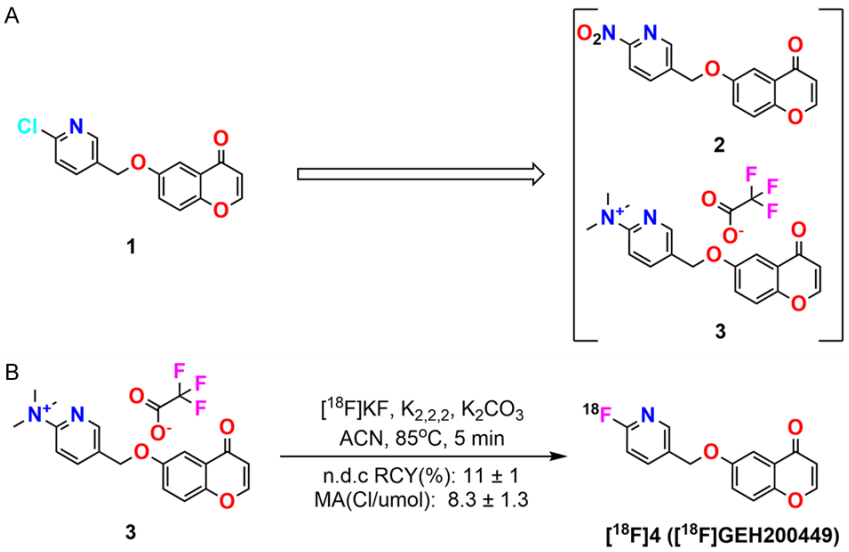


**Figure 1.** Optimization of radiolabeling. A. Chemical structures of labeling precursors 1, 2, and 3. B. Radiosynthesis of compound 3 with fluorine-18.

*In vivo micro PET/CT imaging studies with rodents*

PET/CT imaging was performed on an IRIS small-animal PET/CT system (inviscan SAS, France). Sprague-Dawley rats were anesthetized with 2.5-3% isoflurane and maintained at 37°C using a heated air-circulation system. The radiotracer (15-25 MBq in 150-200 μL saline) was injected intravenously via a tail vein catheter, and dynamic emission scans were acquired in three-dimensional list mode for 60 min. Images were reconstructed and co-registered to an MRI rat brain template using PMOD software (v4.1). Time-activity curves (TACs) were generated from volumes of interest (VOIs) encompassing the cortex, striatum, hippocampus, thalamus, and cerebellum. Radioactivity uptake was expressed as standardized uptake value (SUV), calculated as tissue radioactivity concentration (kBq/mL) divided by injected dose (kBq), multiplied by body weight (g). C57BL/6 mice received 5-10 MBq of tracer in 150-200 μL saline via the tail vein under 1.5-2% isoflurane anesthesia. Imaging and analysis protocols were identical to those used in rats.

*Blocking agent administration*

For pre-blocking studies, the irreversible MAO-B inhibitor L-deprenyl was administered before tracer injection. Briefly, L-deprenyl (2.0-2.5 mg) was dissolved in 0.5 mL of DMSO, and 0.5 mL of Tween-80 was added dropwise under gentle mixing. The mixture was then diluted gradually with water to a final volume of 10 mL to obtain the pre-blocking agent. This agent was further diluted 10-fold with the same solvent mixture (DMSO/Tween-80/water, 0.5:0.5:9, v/v/v) to achieve a concentration of 0.02 mg/mL. Ten minutes prior to PET scanning, mice (20-25 g body weight) were injected via the tail vein with 0.1 mL of the agent at a constant rate.

*Statistical analysis*

All statistical analyses were performed using GraphPad Prism 9.5.0 (GraphPad Software, La Jolla, CA, USA). Data are reported as mean ± standard error of the mean (SEM). Comparisons between groups were made using one-way analysis of variance (ANOVA). Statistical significance was defined as $P < 0.05$, with thresholds indicated as ****$P < 0.0001$.

## Results

*Radiochemical synthesis of [$^{18}$F]4 and optimization of radiolabeling*

Initial radiosynthesis followed the previously reported procedures using precursor 1 [24]. A comprehensive optimization was carried out to evaluate the effects of base selection, solvent effects, reaction temperature, and reaction time on radiochemical yield (RCY) for [$^{18}$F]4. Despite extensive parameter screening (Supplementary Information), the reactions did not provide adequate RCY or satisfactory radiochemical purity. These limitations prompted structural modification of the precursor scaffold, leading to the design and synthesis of novel precursors 2 and 3 (**Figure 1A**). Subsequent refinement of radiolabeling conditions with precursor 3 enabled the successful synthesis of [$^{18}$F]4 with markedly improved efficiency (**Figure 1B**). The final tracer was obtained in 11 ± 1% n.d.c. RCY, with high molar activity of 303.4 ± 48.1 GBq/μmol (8.3 ± 1.3 Ci/μmol) and radiochemical purity > 99%.

*Neuroimaging with [$^{18}$F]4 in rat brains*

The in vivo pharmacokinetic profile of [$^{18}$F]4 was first evaluated in SD rats. Representative whole-brain PET images (transverse, sagittal, and coronal views; 0-60 min) and the corresponding TACs are shown in **Figure 2A** and **2B**, respectively. [$^{18}$F]4 exhibited rapid brain uptake with peak radioactivity observed within 1 min post-injection (SUV = 1.8-4.2) across all brain regions, followed by fast washout. This result confirmed efficient BBB penetration and fast tracer kinetics. However, brain uptake was homogeneous in rats, showing no region-specific binding in contrast to prior reports [24, 26]. We hypothesized that if this discrepancy was caused by species difference, especially different metabolic profile of [$^{18}$F]4, which led to the subsequent radiometabolite analysis study.

*Radiometabolite analysis of [$^{18}$F]4*

To evaluate in vivo metabolic stability of [$^{18}$F]4, radiometabolite analyses were performed in plasma and brain tissues of SD rats at 20 and 60 min post-injection. As

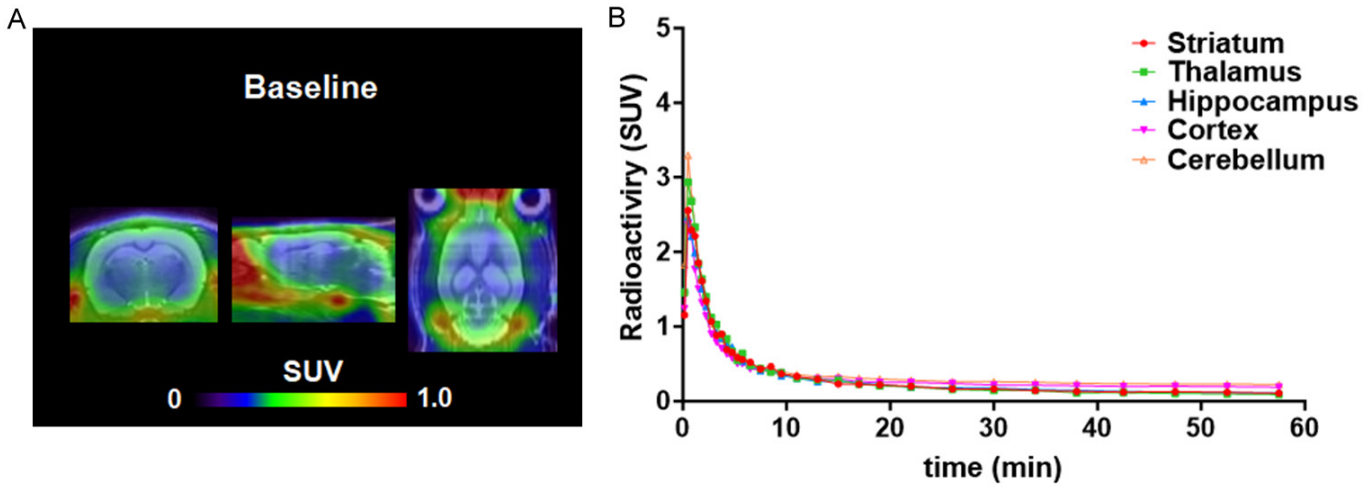


**Figure 2.** In vivo cerebral PET imaging of [$^{18}$F]4 in rats. A, B. Representative fusion images of PET and MRI (0-60 min) and associated kinetic profiles from selected brain regions of rats at baseline.

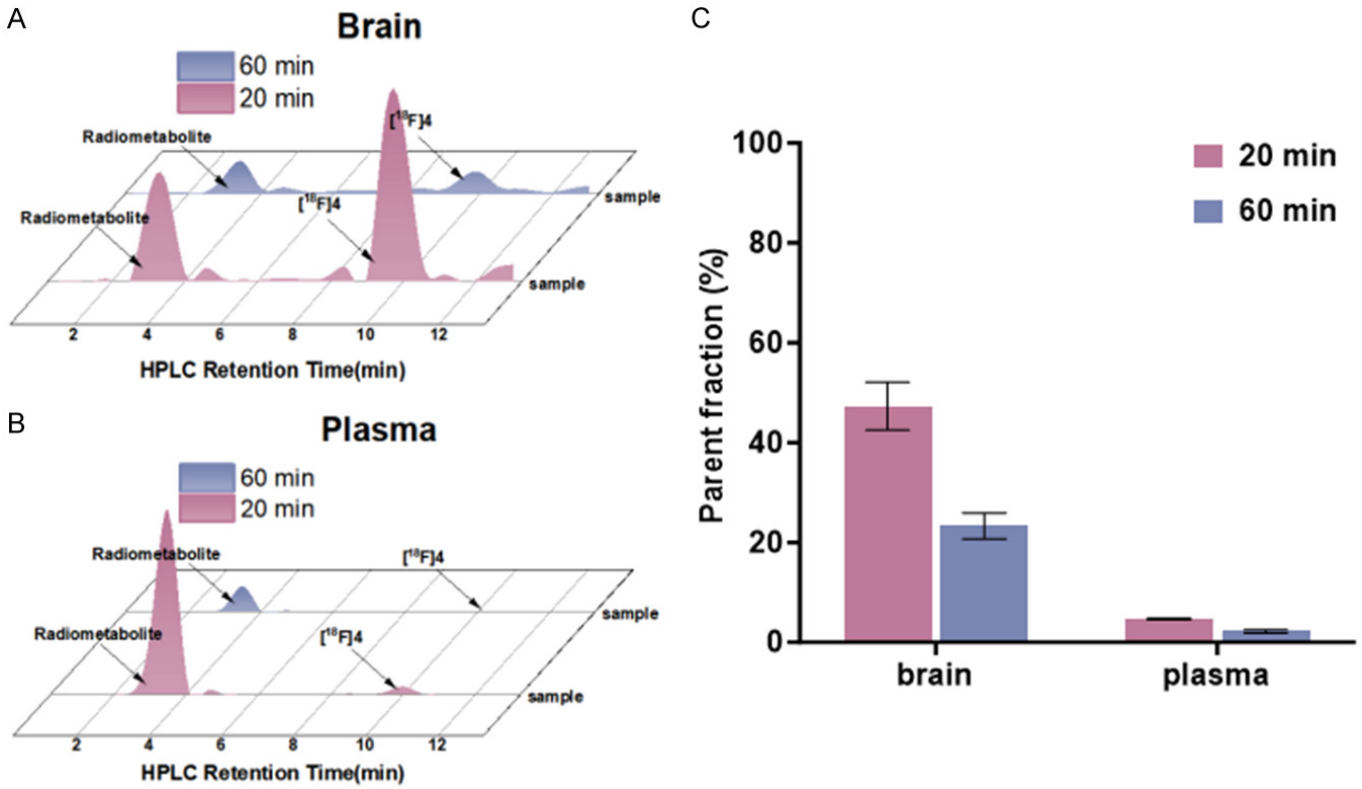


**Figure 3.** Metabolite analysis of [$^{18}$F]4 in rat plasma and brain. A. Representative radio-HPLC traces in the brain. B. Representative radio-HPLC traces in the plasma. C. Percentage of the parent compound [$^{18}$F]4. Data are expressed as mean (n = 3).

shown in **Figure 3**, its metabolic stability in the brain was only moderate. The parent fraction accounted for approximately 47% of total brain radioactivity at 20 min post-injection, declining to 23% by 60 min, indicating rapid degradation. In plasma, metabolic instability was even more pronounced, with parent fractions of 5% and 2% at 20 and 60 min, respectively. Notably, a distinct radiometabolite fraction at a consistent retention time in both plasma and brain samples. This co-eluting metabolite profile strongly suggests that radiometabolites generated in the plasma are capable of crossing the BBB. These brain-penetrant metabolites within the CNS likely contributes to the nonspecific binding, which would interfere with the accurate quantification of target-specific signal. These results demonstrated that [$^{18}$F]4 lacked sufficient in vivo metabolic stability for reliable CNS imaging.

To address this limitation, we employed a deuterium substitution strategy to exploit the kinetic isotope effect (KIE) [27], which has been shown to enhance metabolic stabil-

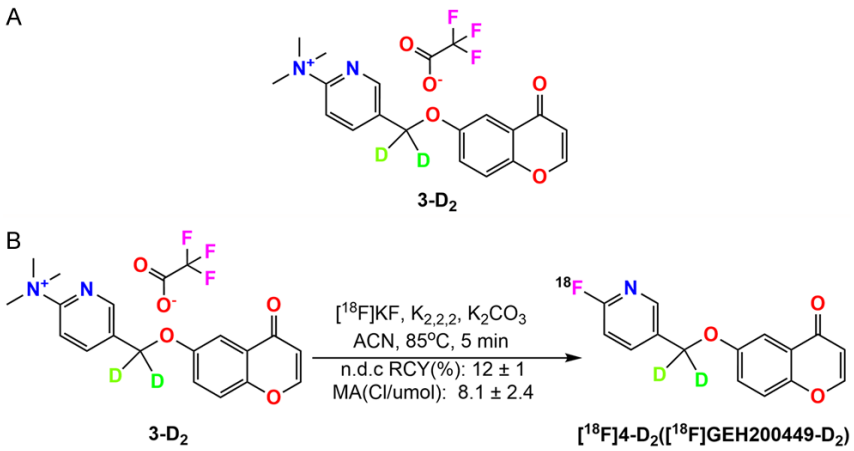


**Figure 4.** Radiolabeling of [$^{18}$F]4-$D_2$. (A) Structures of the precursor 3-$D_2$ and (B) Radiosynthesis of [$^{18}$F]4-$D_2$. [$^{18}$F]fluoride (185-370 MBq; 5-10 mCi) was reacted with 3-$D_2$ (2 mg) in acetonitrile (1.0 mL) in the presence of $K_2CO_3$ (6.0 mg) and Kryptofix 222 (20.0 mg) at 85 °C for 5 min.

ity of PET radiotracers, such as L-[$^{11}$C]Deprenyl-$D_2$ [20], [$^{18}$F]Fluororasagiline-$D_2$ [23], [$^{18}$F]Fluorodeprenyl-$D_2$ [25], [$^{18}$F]$D_2$-LW223 [28], and [$^{18}$F]$D_4$-FET [29]. Accordingly, synthesis of the deuterated analog [$^{18}$F]4-$D_2$ was proposed to evaluate whether reduced radiometabolite formation would improve cerebral pharmacokinetics and enable detection of underlying region-specific MAO-B binding.

*Radiochemical synthesis of [$^{18}$F]4-$D_2$*

The production of [$^{18}$F]4-$D_2$ was carried out on a GE TRACERlab® FX2 N synthesis module (**Figure 4**). The automated synthesis (approximately 100 minutes) afforded the radiotracer in 12 ± 1% n.d.c. RCY, more than 99% radiochemical purity with high molar activity (299.7 ± 88.8 GBq/μmol; 8.1 ± 2.4 Ci/μmol). The identity and purity of the product were confirmed by analytical HPLCs using co-injection with the reference standard.

*Neuroimaging with [$^{18}$F]4-$D_2$ in rodent brains*

To systematically characterize in vivo pharmacokinetics of [$^{18}$F]4-$D_2$, dynamic PET imaging was performed in rodents (mice and rats: 0-60 min). In mice (**Figure 5A** and **5B**), [$^{18}$F]4-$D_2$ demonstrated rapid brain penetration, with TACs from all brain regions peaking within 1 minute (SUV: 2.1-4.1) post injection, followed by steep washout. Comparable kinetics (**Figure 5C** and **5D**) were observed in rats, with peak SUV (2.1-4.6) observed within 1 minute. These cross species PET studies confirmed that [$^{18}$F]4-$D_2$ readily crosses the BBB and exhibits rapid clearance. Homogeneous distribution of radioactivity was observed across all brain regions in PET studies, suggesting that the specific binding of the parent tracer is likely to be obscured by non-specific binding. Subsequently, we conducted a pre-blocking experiment in mice using L-deprenyl. As shown in **Figure 5E** and **5F**, no significant difference was observed in the cerebral TACs before and after blockade, further indicating the lack of MAO-B-specific binding of [$^{18}$F]4-$D_2$ in rodents.

*Radiometabolite analysis of [$^{18}$F]4-$D_2$*

To assess in vivo metabolic stability of the deuterated radiotracer [$^{18}$F]4-$D_2$, ex vivo metabolite analyses were performed in rat plasma and brain at 20 and 60 min after intravenous injection. The radiometabolite distribution profiles were presented in **Figure 6**. Radiochromatograms of brain homogenates (**Figure 6A**) revealed multiple peaks as radiometabolites, in addition to the primary peak corresponding to intact [$^{18}$F]4-$D_2$. Quantitative analysis indicated substantial metabolic degradation, with the parent fraction representing 54% of total brain radioactivity at 20 minutes and declining sharply to 15% by 60 minutes (**Figure 6C**). Plasma chromatograms (**Figure 6B**) demonstrated even greater instability, characterized by a major radiometabolite peak. The parent fraction in the plasma was markedly lower than in brain tissue, measuring 4.5% at 20 minutes and decreasing further to 3.0% at 60 minutes (**Figure 6C**). The rapid degradation observed in both CNS and peripheral compartments, as reflected by the pronounced decline in parent tracer fractions, indicated that our deuteration strategy failed to achieve the desired resistance to oxidative metabolism.

*Revisit binding specificity in vitro*

The inconsistent performance of the parent compound [$^{18}$F]4 relative to previously reported data prompted a re-evaluation of the binding specificity of its deuterated analog [$^{18}$F]4-$D_2$. In vitro autoradiography on rat brain sections (**Figure 7**) was performed to evaluate the binding specificity of [$^{18}$F]4-$D_2$ for MAO-B. Quantitative analysis (**Figure 6D**) showed high baseline signal intensity (1853 ± 655 PSI/mm$^2$), confirming robust tracer binding under control conditions. Pre-treatment with the MAO-A inhibitor pirlindole substantially reduced the signal (212 ± 28 PSL/mm$^2$; ****P < 0.0001), whereas blockade with the MAO-B inhibitor L-deprenyl resulted in an even greater reduction (120 ± 13 PSL/mm$^2$; ****P ≤ 0.0001). These results demonstrated that [$^{18}$F]4-$D_2$ binding was displaced by both MAO-A and MAO-B inhibitors, indicating substantial off-target interaction with MAO-A and insufficient isoform selectivity for MAO-B. This insufficient selectivity further compounded this scaffold's deficiencies.

## Discussions

This study provides a comprehensive in vivo evaluation of the novel fluorine-18 labeled tracer [$^{18}$F]4 and its deuterated analogue [$^{18}$F]4-$D_2$ for imaging MAO-B in rodents.

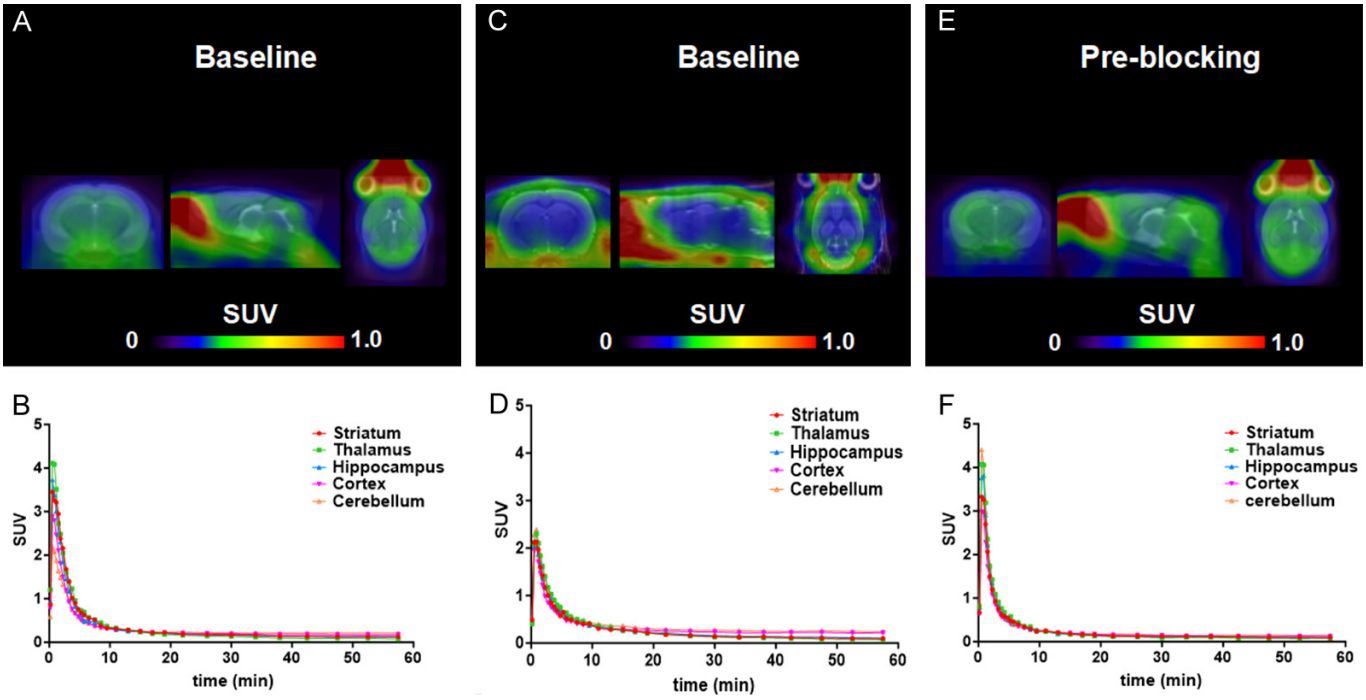


**Figure 5.** In vivo cerebral PET imaging of [$^{18}$F]4-$D_2$ in the mouse, rat. A, B. Representative fusion images of PET and MRI (0-60 min) and associated kinetic profiles from selected brain regions of mice at baseline; C, D. Representative fusion images of PET and MRI (0-60 min) and associated kinetic profiles from selected brain regions of rats at baseline; E, F. Representative fusion images of PET and MRI (0-60 min) and associated kinetic profiles from selected brain regions of mice at pre-blocking.

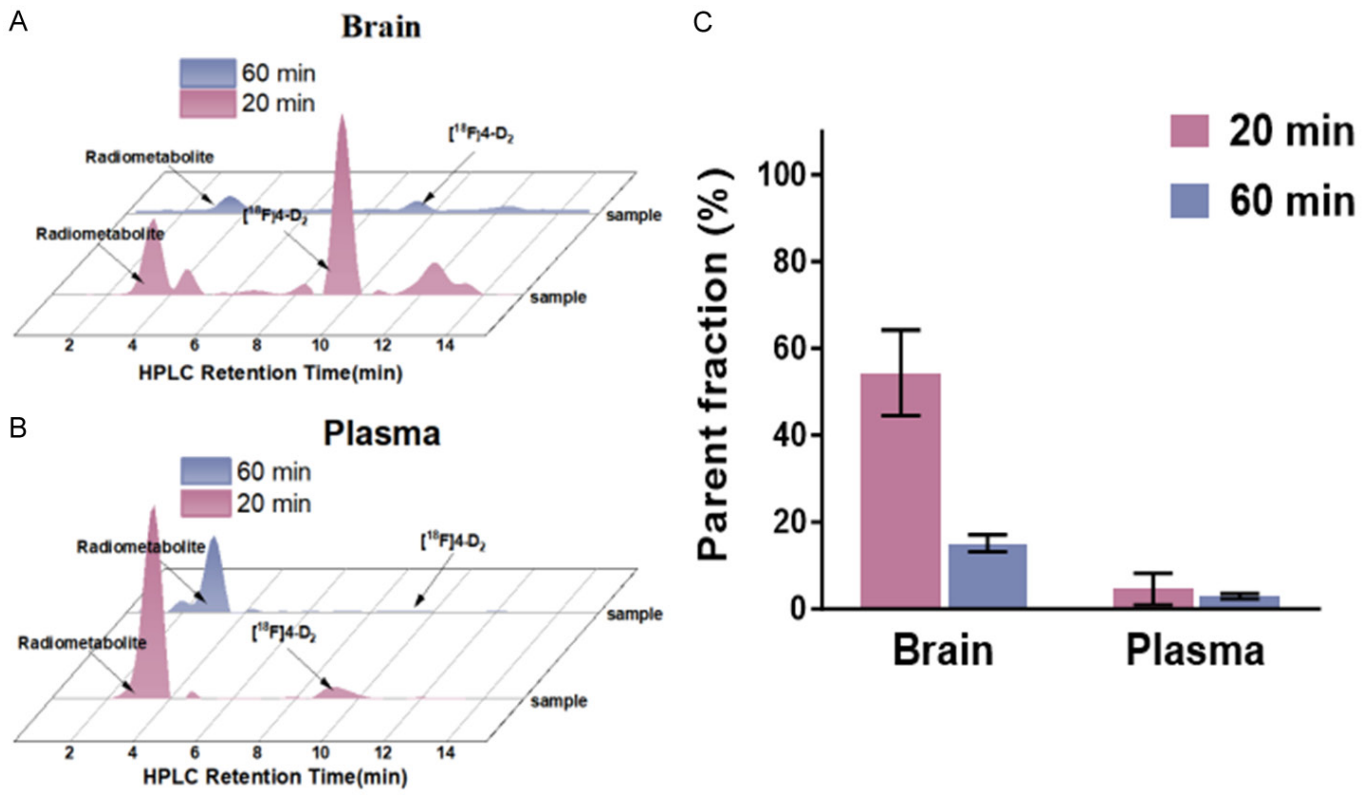


**Figure 6.** Metabolite analysis of [$^{18}$F]4-$D_2$ in rat plasma and brain at 20 and 60 min after intravenous injection. A. Reconstructed radio-HPLC traces of cerebral samples. B. Reconstructed radio-HPLC traces of plasma, demonstrating two separate radiometabolite peaks. C. Percentage of the compound [$^{18}$F]4-$D_2$. Data are expressed as mean (n = 3).

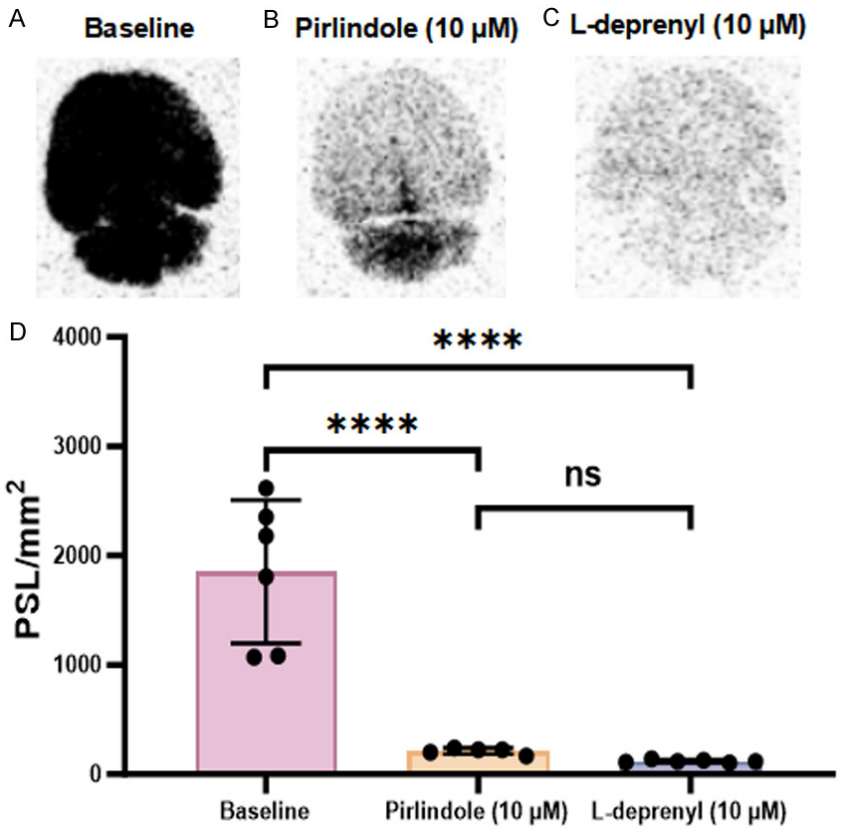


**Figure 7.** Assessment of [$^{18}$F]4-$D_2$ binding specificity in rat brain tissue using in vitro autoradiography. (A) Total binding after 90-min incubation with the radiotracer alone. (B, C) Blocking studies with the addition of 10 μM pirlindole (B) or 10 μM L-deprenyl (C). (D) Quantification of specific binding under baseline and blocked conditions. Data are expressed as mean ± SEM (Baseline: $n$ = 6; Pirlindole: $n$ = 5; L-deprenyl: $n$ = 6) and assessed by one-way ANOVA; **** denotes $P \leq 0.0001$.

While both radiotracers exhibited rapid and efficient BBB penetration - a fundamental prerequisite for CNS imaging agents - they failed to demonstrate region-specific retention patterns consistent with the known heterogeneous distribution of MAO-B in the brain. This homogeneous signal, observed across rodent models, stands in contrast to prior reports highlighting the selective binding of [$^{18}$F]4 in human brain sections and NHPs [24, 26]. The discrepancy suggests potential species-dependent differences in tracer metabolism or off-target interactions that become predominant in rodents, overshadowing specific MAO-B binding.

A central finding was the pronounced metabolic instability of the parent scaffold. Ex vivo metabolite analysis revealed extensive degradation of [$^{18}$F]4 in both plasma and brain, generating radiometabolites capable of crossing the BBB. These brain-penetrant metabolites contribute to a confounding background signal, compromising the accurate quantification of target-specific binding. To address this, we employed a deuteration strategy, a well-established approach to retard oxidative metabolism via the KIE [27]. Surprisingly, the comprehensive pharmacokinetic and metabolite profile of [$^{18}$F]4-$D_2$ indicated that deuteration at the chosen position failed to confer the anticipated metabolic resilience. The rapid and near-identical degradation profiles of both tracers imply that deuteration at the benzylic α-position did not interfere with the primary metabolic pathway. We propose the following specific mechanistic hypotheses to explain the failure of the KIE: (I) The deuterated site may not be the primary locus of oxidative attack. Other vulnerable positions on the molecule, such as aromatic rings or α-positions to nitrogen atoms, might serve as preferential targets for drug-metabolizing enzymes. (II) More likely, non-oxidative metabolic pathways insensitive to KIE may predominate. Given the presence of a lactone ring in the molecular scaffold, enzymatic hydrolysis of the ester bond by esterases emerges as a prime candidate. This hydrolytic ring-opening represents a common and rapid in vivo clearance route for lactone-containing compounds and is entirely independent of C-H bond cleavage, rendering it unaffected by deuterium substitution. The resulting open-chain metabolites could undergo alterations in polarity, conformation, and binding properties, likely contributing significantly to the observed metabolite peaks and the confounding nonspecific brain signal. Furthermore, if the metabolites contain phenolic hydroxyl or amine groups, they may undergo subsequent Phase II reactions. These conjugation processes are also insensitive to deuterium substitution and typically yield metabolites with increased polarity.

Furthermore, in vitro autoradiography delivered a critical insight into the scaffold's selectivity. The binding of [$^{18}$F]4-$D_2$ was substantially displaced not only by the MAO-B inhibitor L-deprenyl but also by the MAO-A inhibitor pirlindole. This result demonstrates a significant lack of isoform selectivity, revealing substantial off-target binding to MAO-A. The lack of isoform selectivity for [$^{18}$F]4-$D_2$, which stands in striking contrast to the reported MAO-B selectivity of its parent compound [$^{18}$F]4 in human post-mortem tissue. This discrepancy warrants deeper investigation. Several factors could contribute to the observed divergence. First, and most plausibly, species differences between rodents and primates in the molecular conformation, relative abundance, and physiological roles of MAO-A and MAO-B may lead to altered binding profiles of the same ligand. For instance, the substrate and inhibitor preferences of human MAO-A and MAO-B are determined neither by the corresponding Phe208/Ile199 residues found in rat MAO nor by their adjacent region [30]. Such interspecies divergence likely explains why a ligand exhibiting relative selectivity in primates may demonstrate

more pronounced cross-reactivity with both isoforms in rodents. The inhibitor concentration used (10 μM) was sufficient for effective blockade in our rat model, as evidenced by the significant displacement achieved with both L-deprenyl and pirlindole. This strongly supports the conclusion that [$^{18}$F]4-$D_2$ binds appreciably to both MAO-A and MAO-B in the rat brain. While subtle batch-to-batch variability in the tracer cannot be entirely ruled out, rigorous quality control makes this an unlikely primary cause. Therefore, the data strongly suggest that the [$^{18}$F]4/[$^{18}$F]4-$D_2$ scaffold possesses an inherent, species-modulated affinity for both MAO isoforms, which becomes prominently exposed in the rodent brain. This insufficient selectivity, combined with the inherent metabolic instability, represents a dual deficiency that fundamentally limits the utility of this chemical series for specific MAO-B imaging. Our findings thus extend upon previous literature: while the scaffold shows promise in specific NHP contexts [26], its performance in rodents underscores vulnerabilities - particularly in metabolic stability and selectivity - that could critically impact its reliability in human translational studies. Our work reinforces the critical importance of conducting thorough in vivo metabolite analysis and blocking studies in relevant animal models early in the tracer development pipeline to identify such confounding factors before costly human translation.

Although radiometabolite structural identification was not performed in this study, the following specific pathways, known to exhibit significant interspecies variation, offer plausible explanations: First, divergent cytochrome P450 (CYP450) enzyme profiles between species could alter the site or efficiency of oxidative metabolism. Primates predominantly rely on CYP3A4/5, whereas rodents express distinct, sex-dimorphic CYP3A isoforms with different catalytic properties [31-34]. It is conceivable that oxidative attack on [$^{18}$F]4-$D_2$ in rodents occurs at a position not protected by deuteration, or is mediated by a non-CYP3A4/5 enzyme, nullifying the KIE strategy. More compellingly, non-oxidative pathways insensitive to KIE likely play a predominant role in rodents. The lactone ring within [$^{18}$F]4-$D_2$ is highly susceptible to hydrolysis by esterases, a reaction independent of C-H bond cleavage. Notable species differences in esterase activity and isoform distribution suggest that this hydrolytic pathway may be particularly efficient in rodents, leading to rapid ring-opening and clearance [35, 36]. Furthermore, significant interspecies disparities in Phase II conjugation enzymes, such as UDP-glucuronosyltransferases (UGTs) [37, 38]. If [$^{18}$F]4-$D_2$ serves as a favorable substrate for specific, highly active UGT isoforms in rodents, it may undergo rapid conjugation, leading to the formation of polar metabolites. Such conjugation reactions are likewise unaffected by the KIE. Therefore, the combined action of potentially robust esterase-mediated hydrolysis and efficient Phase II conjugation in rodents provides a coherent hypothesis for the rapid degradation of [$^{18}$F]4-$D_2$ and the failure of deuteration observed in this study. This contrasts with a potentially greater reliance on oxidative pathways in NHPs, aligning with the more favorable metabolic profile reported previously [26].

In light of the aforementioned limitations, the focus of future work should center on systematically evaluating the dual impact of all structural modifications on both metabolic stability and isoform selectivity. First, precise metabolic profiling of [$^{18}$F]4/[$^{18}$F]4-$D_2$ via high-resolution mass spectrometry is essential to identify metabolic soft spots and the predominant pathways. Guided by this knowledge, the following rational structural modifications can be pursued: if oxidation at specific C-H bonds is confirmed, targeted or multi-site deuteration can be implemented. Alternatively, introducing more effective sterically hindering or electron-withdrawing groups at the metabolic soft spots can directly block enzyme binding or catalysis. Notably, recent structural optimization studies of second-generation hMAO-B inhibitors, such as safinamide, have demonstrated that strategies including cyclization, incorporation of benzofuran rings, fluorination, and ring expansion can significantly enhance drug potency, metabolic stability, and isoform selectivity [39, 40]. If optimization of the current molecular scaffold proves unfeasible, a de novo design strategy based on pharmacophores from other high-selectivity MAO-B inhibitors will be pursued.

Several limitations of this study should be acknowledged. Our evaluation was primarily conducted in rodents. While this is a standard early-stage screening model, the observed species differences in tracer performance highlight that data from rats and mice may not fully predict behaviour in higher-order species, including humans. The definitive assessment of tracer selectivity would also benefit from complementary studies in MAO-B knockout models.

## Conclusions

This study systematically characterized the MAO-B PET tracer candidate [$^{18}$F]4 and its deuterated analogue [$^{18}$F]4-$D_2$. Although [$^{18}$F]4 exhibited favorable BBB penetration, it underwent extensive metabolic degradation in both plasma and brain compartments, generating brain-penetrant radiometabolites that confounded signal interpretation. Deuterium substitution in [$^{18}$F]4-$D_2$ was intended to mitigate this instability, but comprehensive evaluations confirmed that deuteration failed to resolve the scaffold's two major shortcomings: (1) metabolic instability and (2) insufficient isoform selectivity due to substantial off-target MAO-A binding. Despite efficient BBB penetration across rodents, these deficiencies preclude its use as a quantitative and selective MAO-B imaging agent. Future optimization should extend beyond deuteration to rational pharmacophore redesign, incorporating metabolically robust functional groups and systematic structure-activity relationship (SAR) studies to improve both stability and selectivity. Such refinements may enable the devel-

opment of next-generation MAO-B PET ligands with genuine translational potential for clinical neuroimaging.

## Acknowledgements

We would like to thank the staff at the radiochemistry program at the Department of Nuclear Medicine, the First Affiliated Hospital of Jinan University for their support with cyclotron operation and radioisotope production. This work was supported by the National Natural Science Foundation of China (Nos. 82572296, 82371998), Open Program at Guangdong Provincial Key Laboratory of Research on Emergency in TCM (2023B1212060062), and Construction Project of Shanghai Key Laboratory of Molecular Imaging (18DZ2260400).

## Disclosure of conflict of interest

None.

**Address correspondence to:** Hao Xu and Lu Wang, State Key Laboratory of Bioactive Molecules and Druggability Assessment, Guangdong Basic Research Center of Excellence for Natural Bioactive Molecules and Discovery of Innovative Drugs, Department of Nuclear Medicine, The First Affiliated Hospital, Jinan, China. E-mail: txh@jnu.edu.cn (HX); l_wang1009@foxmail.com (LW)

## References

[1] Riederer P, Konradi C, Schay V, Kienzl E, Birkmayer G, Danielczyk W, Sofic E and Youdim MB. Localization of MAO-A and MAO-B in human brain: a step in understanding the therapeutic action of L-deprenyl. Adv Neurol 1987; 45: 111-118.

[2] Shih JC, Chen K and Ridd MJ. Monoamine oxidase: from genes to behavior. Annu Rev Neurosci 1999; 22: 197-217.

[3] Youdim MB and Bakhle YS. Monoamine oxidase: isoforms and inhibitors in Parkinson's disease and depressive illness. Br J Pharmacol 2006; 147 Suppl 1: S287-296.

[4] Jossan SS, Hiraga Y and Oreland L. The cholinergic neurotoxin ethylcholine mustard aziridinium (AF64A) induces an increase in MAO-B activity in the rat brain. Brain Res 1989; 476: 291-297.

[5] Tetrud JW and Langston JW. The effect of deprenyl (selegiline) on the natural history of Parkinson's disease. Science 1989; 245: 519-522.

[6] Jossan SS, Gillberg PG, Gottfries CG, Karlsson I and Oreland L. Monoamine oxidase B in brains from patients with Alzheimer's disease: a biochemical and autoradiographical study. Neuroscience 1991; 45: 1-12.

[7] Gerlach M, Desser H, Youdim MB and Riederer P. New horizons in molecular mechanisms underlying Parkinson's disease and in our understanding of the neuroprotective effects of selegiline. J Neural Transm Suppl 1996; 48: 7-21.

[8] Mészáros Z, Borcsiczky D, Máté M, Tarcali J, Szombathy T, Tekes K and Magyar K. Platelet MAO-B activity and serotonin content in patients with dementia: effect of age, medication, and disease. Neurochem Res 1998; 23: 863-868.

[9] Robinson DS, Nies A, Davis JN, Bunney WE, Davis JM, Colburn RW, Bourne HR, Shaw DM and Coppen AJ. Ageing, monoamines, and monoamine-oxidase levels. Lancet 1972; 1: 290-291.

[10] Oreland L. Monoamine oxidase, dopamine and Parkinson's disease. Acta Neurol Scand Suppl 1991; 136: 60-65.

[11] Carter SF, Herholz K, Rosa-Neto P, Pellerin L, Nordberg A and Zimmer ER. Astrocyte biomarkers in Alzheimer's disease. Trends Mol Med 2019; 25: 77-95.

[12] Sofroniew MV. Astrocyte reactivity: subtypes, states, and functions in CNS innate immunity. Trends Immunol 2020; 41: 758-770.

[13] Jaisa-Aad M, Muñoz-Castro C, Healey MA, Hyman BT and Serrano-Pozo A. Characterization of monoamine oxidase-B (MAO-B) as a biomarker of reactive astrogliosis in Alzheimer's disease and related dementias. Acta Neuropathol 2024; 147: 66.

[14] Yamada M and Yasuhara H. Clinical pharmacology of MAO inhibitors: safety and future. Neurotoxicology 2004; 25: 215-221.

[15] Fariello RG and Lieberman A. Present and future approaches to Parkinson disease: from molecular insights to new therapeutic avenues. Neurology 2006; 67 Suppl 2: S1-4.

[16] Schedin-Weiss S, Inoue M, Hromadkova L, Teranishi Y, Yamamoto NG, Wiehager B, Bogdanovic N, Winblad B, Sandebring-Matton A, Frykman S and Tjernberg LO. Monoamine oxidase B is elevated in Alzheimer disease neurons, is associated with γ-secretase and regulates neuronal amyloid β-peptide levels. Alzheimers Res Ther 2017; 9: 57.

[17] Ametamey SM, Honer M and Schubiger PA. Molecular imaging with PET. Chem Rev 2008; 108: 1501-1516.

[18] Fang Y, Chen Z and Yang M. Small molecule probes for the specific imaging of monoamine oxidase A and monoamine oxidase B. Iradiology 2024; 2: 191-215.

[19] Fowler JS, MacGregor RR, Wolf AP, Arnett CD, Dewey SL, Schlyer D, Christman D, Logan J, Smith M and Sachs H. Mapping human brain monoamine oxidase A and B with 11C-labeled suicide inactivators and PET. Science 1987; 235: 481-485.

[20] Fowler JS, Wang GJ, Logan J, Xie S, Volkow ND, MacGregor RR, Schlyer DJ, Pappas N, Alexoff DL and Patlak C. Selective reduction of radiotracer trapping by deuterium substitution: comparison of carbon-11-L-deprenyl and carbon-11-deprenyl-D2 for MAO B mapping. J Nucl Med 1995; 36: 1255-1262.

[21] Rusjan PM, Wilson AA, Miler L, Fan I, Mizrahi R, Houle S, Vasdev N and Meyer JH. Kinetic modeling of the monoamine oxidase B radioligand [$^{11}$C]SL25.1188 in human brain with high-resolution positron emission tomography. J Cereb Blood Flow Metab 2014; 34: 883-889.

[22] Nag S, Lehmann L, Kettschau G, Heinrich T, Thiele A, Varrone A, Gulyas B and Halldin C. Synthesis and evaluation of [$^{18}$F]fluororasagiline, a novel positron emission tomography (PET) radioligand for monoamine oxidase B (MAO-B). Bioorg Med Chem 2012; 20: 3065-3071.

[23] Nag S, Lehmann L, Kettschau G, Toth M, Heinrich T, Thiele A, Varrone A and Halldin C. Development of a novel fluorine-18 labeled deuterated fluororasagiline ([(18)F]fluororasagiline-D2) radioligand for PET studies of monoamino oxidase B (MAO-B). Bioorg Med Chem 2013; 21: 6634-6641.

[24] Nag S, Jia Z, Svedberg M, Jackson A, Ahmad R, Luthra S, Varnäs K, Farde L and Halldin C. Synthesis and autoradiography of novel F-18 labeled reversible radioligands for detection of monoamine oxidase B. ACS Chem Neurosci 2020; 11: 4398-4404.

[25] Nag S, Fazio P, Lehmann L, Kettschau G, Heinrich T, Thiele A, Svedberg M, Amini N, Leesch S, Catafau AM, Hannestad J, Varrone A and Halldin C. In vivo and in vitro characterization of a novel MAO-B inhibitor radioligand, 18F-labeled deuterated fluorodeprenyl. J Nucl Med 2016; 57: 315-320.

[26] Varnäs K, Nag S, Halldin C and Farde L. PET Evaluation of the novel F-18 labeled reversible radioligand [(18)F] GEH200449 for detection of monoamine oxidase-B in the non-human primate brain. ACS Chem Neurosci 2023; 14: 3206-3211.

[27] Klenner MA, Pascali G, Fraser BH and Darwish TA. Kinetic isotope effects and synthetic strategies for deuterated carbon-11 and fluorine-18 labelled PET radiopharmaceuticals. Nucl Med Biol 2021; 96-97: 112-147.

[28] Liao K, Chen JH, Ma J, Dong CC, Bi CY, Gao YB, Jiang YF, Wang T, Wei HY, Hou L, Hu JQ, Wei JJ, Zeng CY, Li YL, Yan S, Xu H, Liang SH and Wang L. Preclinical characterization of [(18)F]D(2)-LW223: an improved metabolically stable PET tracer for imaging the translocator protein 18 kDa (TSPO) in neuroinflammatory rodent models and non-human primates. Acta Pharmacol Sin 2025; 46: 393-403.

[29] Hou L, Chen Z, Chen F, Sheng L, Ye W, Dai Y, Guo X, Dong C, Li G, Liao K, Li Y, Ma J, Wei H, Ran W, Shang J, Ling X, Patel JS, Liang SH, Xu H and Wang L. Synthesis, preclinical assessment, and first-in-human study of [(18)F]d(4)-FET for brain tumor imaging. Eur J Nucl Med Mol Imaging 2025; 52: 864-875.

[30] Geha RM, Chen K and Shih JC. Phe(208) and Ile(199) in human monoamine oxidase A and B do not determine substrate and inhibitor specificities as in rat. J Neurochem 2000; 75: 1304-1309.

[31] Woodland C, Huang TT, Gryz E, Bendayan R and Fawcett JP. Expression, activity and regulation of CYP3A in human and rodent brain. Drug Metab Rev 2008; 40: 149-168.

[32] Anakk S, Kalsotra A, Kikuta Y, Huang W, Zhang J, Staudinger JL, Moore DD and Strobel HW. CAR/PXR provide directives for Cyp3a41 gene regulation differently from Cyp3a11. Pharmacogenomics J 2004; 4: 91-101.

[33] Matsubara T, Kim HJ, Miyata M, Shimada M, Nagata K and Yamazoe Y. Isolation and characterization of a new major intestinal CYP3A form, CYP3A62, in the rat. J Pharmacol Exp Ther 2004; 309: 1282-1290.

[34] Nelson DR. Cytochrome P450: Structure, Mechanism, and Biochemistry, 3rd ed Edited by Paul R. Ortiz de Montellano (University of California, San Francisco). Kluwer Academic/Plenum Publishers: New York. 2005. xx + 690 pp. $149.00. ISBN 0-306-48324-6. J Am Chem Soc 2005; 127: 12147-12148.

[35] Bahar FG, Ohura K, Ogihara T and Imai T. Species difference of esterase expression and hydrolase activity in plasma. J Pharm Sci 2012; 101: 3979-3988.

[36] Godin SJ, Scollon EJ, Hughes MF, Potter PM, DeVito MJ and Ross MK. Species differences in the in vitro metabolism of deltamethrin and esfenvalerate: differential oxidative and hydrolytic metabolism by humans and rats. Drug Metab Dispos 2006; 34: 1764-1771.

[37] Fujiwara R, Yoda E and Tukey RH. Species differences in drug glucuronidation: humanized UDP-glucuronosyltransferase 1 mice and their application for predicting drug glucuronidation and drug-induced toxicity in humans. Drug Metab Pharmacokinet 2018; 33: 9-16.

[38] Oda S, Fukami T, Yokoi T and Nakajima M. A comprehensive review of UDP-glucuronosyltransferase and esterases for drug development. Drug Metab Pharmacokinet 2015; 30: 30-51.

[39] Yi C, Liu X, Chen K, Liang H and Jin C. Design, synthesis and evaluation of novel monoamine oxidase B (MAO-B) inhibitors with improved pharmacokinetic properties for Parkinson's disease. Eur J Med Chem 2023; 252: 115308.

[40] Zhu M, Xie XP, Wang S, Zhang XX, Xie Z, Duan Y, Zhao Z and Liao C. Design, synthesis, and biological evaluation of highly potent and selective hMAO-B inhibitors featuring a tetrahydrobenzo[f][1,4]oxazepine core. Eur J Med Chem 2025; 299: 118080.

# Supplementary Information

## Chemical synthesis

*Synthesis of 6-hydroxy-4H-chromen-4-one (**S2**)*

To a solution of 1-(2,5-dihydroxyphenyl)ethan-1-one **S1** (500 mg, 3.29 mmol) in $HC(OEt)_3$ (3 mL) was added perchloric acid (0.33 mL) dropwise. The mixture was stirred at room temperature for 1 h. TLC showed no SM remaining and LCMS showed desired product. The reaction mixture was added PE (9 mL) and filtrated, collected the filter cake, which was dissolved in hot water and heated at reflux for 5 minutes. The mixture was then allowed to cool to room temperature. The resulting mixture was filtered, and the filter cake was dried to give the 6-hydroxy-4H-chromen-4-one **S2** (290 mg, 54%) as a black solid. $^1$H NMR (400 MHz, DMSO-$d_6$) δ 10.01 (s, 1H), 8.23 (d, *J* = 6.0 Hz, 1H), 7.52 (d, *J* = 9.0 Hz, 1H), 7.30 (d, *J* = 3.0 Hz, 1H), 7.23 (dd, *J* = 9.0, 3.0 Hz, 1H), 6.26 (d, *J* = 5.9 Hz, 1H).

*Synthesis of 6-((6-chloropyridin-3-yl)methoxy)-4H-chromen-4-one (**1**)*

To a solution of 6-hydroxy-4H-chromen-4-one **S2** (100 mg, 0.62 mmol) in acetone (3 mL) was added 2-chloro-5-(chloromethyl) pyridine **S3** (150 mg, 0.93 mmol) and $K_2CO_3$ (214 mg, 1.55 mmol) before stirred at 60°C overnight. TLC showed no SM remaining and LCMS showed desired product. The reaction mixture was concentrated and purified by flash (DCM/MeOH = 20/1) to give 6-((6-chloropyridin-3-yl)methoxy)-4H-chromen-4-one **1** (78.06 mg, 44% for 1 step) as a white solid. LCMS (ESI): m/z, 288.04 [M+H]+, RT = 1.96 min. HPLC: 98%, RT = 5.273 min. $^1$H NMR (400 MHz, DMSO-$d_6$) δ 8.56 (d, *J* = 2.4 Hz, 1H), 8.30 (d, *J* = 6.0 Hz, 1H), 7.99 (dd, *J* = 8.2, 2.5 Hz, 1H), 7.66 (d, *J* = 9.0 Hz, 1H), 7.58 (d, *J* = 8.2 Hz, 1H), 7.54 (d, *J* = 3.1 Hz, 1H), 7.50 (dd, *J* = 9.1, 3.1 Hz, 1H), 6.34 (d, *J* = 6.0 Hz, 1H), 5.29 (s, 2H).

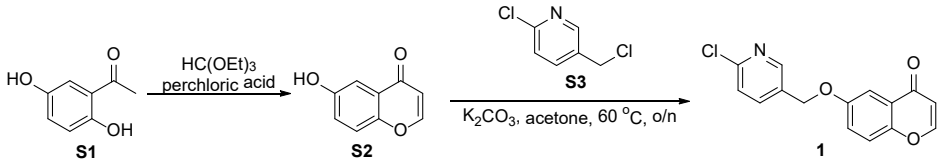


**Scheme 1.** Syntheses of precursor **1**.

*Synthesis of 6-((6-nitropyridin-3-yl)methoxy)-4H-chromen-4-one (**2**)*

To a solution of 6-hydroxy-4H-chromen-4-one **S2** (90 mg, 0.42 mmol) in acetone (4 mL) was added 5-(bromomethyl)-2-nitropyridine **S4** (81 mg, 0.50 mmol) and $K_2CO_3$ (145 mg, 1.05 mmol) before stirred at 60°C overnight. TLC showed no SM remaining and LCMS showed desired product. The reaction mixture was concentrated and purified by flash (PE/EA = 1/1) to give the 6-((6-nitropyridin-3-yl)methoxy)-4H-chromen-4-one **2** (62.47 mg, 50%) as a white solid. LCMS (ESI): m/z, 299.01 [M+H]+, RT = 1.863 min. HPLC: 96%, RT = 5.258 min. $^1$H NMR (400 MHz, DMSO-$d_6$) δ 8.85 - 8.74 (m, 1H), 8.41 - 8.31 (m, 2H), 8.30 (d, *J* = 6.0 Hz, 1H), 7.68 (d, *J* = 9.0 Hz, 1H), 7.62 - 7.51 (m, 2H), 6.35 (d, *J* = 6.0 Hz, 1H), 5.47 (s, 2H).

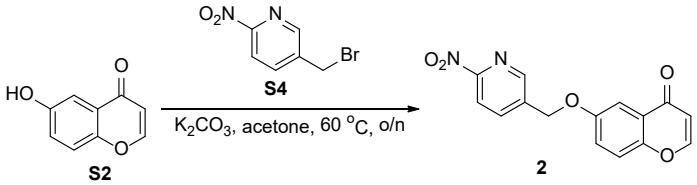


**Scheme 2.** Syntheses of precursor **2**.

*Synthesis of 6-(pyridin-3-ylmethoxy)-4H-chromen-4-one (**S6**)*

To a solution of 6-hydroxy-4H-chromen-4-one **S2** (4.62 g, 28.50 mmol) in acetone (80 mL) was added 3-(chloromethyl)pyridine hydrochloride **S5** (4.25 g, 25.91 mmol) and $K_2CO_3$ (14.32 g, 103.64 mmol). The mixture was stirred at 60°C overnight. TLC showed no SM remaining and LCMS showed desired product. After cooling to room temperature, the reaction was quenched with water (200 mL) and diluted with ethyl acetate (100 mL). The organic layer was separated, and the aqueous layer was extracted with ethyl acetate (2 × 100 mL). The combined organic layers were washed with water, brine, dried over $Na_2SO_4$, filtered, and concentrated in vacuo. The crude product was purified by flash column chromatography (ethyl acetate/petrol = 1:1) on a silica gel to afford the desired product **S6** (5 g, 76% yield) as a yellow solid.

*Synthesis of3-(((4-oxo-4H-chromen-6-yl)oxy)methyl)pyridine 1-oxide (**S7**)*

To a solution of 6-(pyridin-3-ylmethoxy)-4H-chromen-4-one **S6** (5 g, 19.74 mmol) in DCM (100 mL) was added m-CPBA (4.4 g, 21.72 mmol). The mixture was stirred at 25°C overnight. TLC showed 20% SM remaining and LCMS showed desired product. The reaction was quenched with water (200 mL) and diluted with DCM (100 mL). The organic layer was separated, and the aqueous layer was extracted with DCM (2 × 50 mL). The combined organic layers were washed with water, brine, dried over $Na_2SO_4$, filtered, and concentrated in vacuo. The crude product was purified by flash column chromatography (DCM:MeOH = 20:1 to 10:1) on a silica gel to afford the desired product **S7** (4.4 g, 83% yield) as a white solid. $^1$H NMR (400 MHz, DMSO-$d_6$) δ 8.36 (dt, *J* = 1.9, 1.0 Hz, 1H), 8.29 (d, *J* = 6.0 Hz, 1H), 8.19 (dt, *J* = 4.8, 2.4 Hz, 1H), 7.69 - 7.62 (m, 1H), 7.52 (d, *J* = 7.3 Hz, 2H), 7.48 - 7.41 (m, 2H), 6.34 (d, *J* = 6.0 Hz, 1H), 5.24 (s, 2H).

*Synthesis of N,N,N-trimethyl-5-(((4-oxo-4H-chromen-6-yl)oxy)methyl)pyridin-2-aminium 2,2,2-trifluoroacetate EM43A-2-NMe$_3$ (**3**)*

To a solution of 3-(((4-oxo-4H-chromen-6-yl)oxy)methyl)pyridine 1-oxide 4 (2 g, 7.43 mmol) in DCM (40 mL) was added $Me_3N$ (11 mL, 22.28 mmol, 2 M) and TFAA (4.7 g, 22.28 mmol). The mixture was stirred at 25°C overnight. TLC showed much SM remaining and LCMS showed 10% of the desired product. The reaction was concentrated in vacuo to give crude, which was dissolved in $H_2O$, washed with DCM/MeOH = 10:1 (50 mL) for 10 times. The aqueous phase was freezed dry to give crude desired product. The crude desired product was purified by Prep-HPLC (ACN/0.1% TFA in $H_2O$) to afford the desired product (173 mg, 5% yield) as a white solid. LC-MS (+ESI): m/z = 311.2 (M+1), HPLC: 95%, RT = 4.059 min. $^1$H NMR (400 MHz, Chloroform-d) δ 8.64 (s, 1H), 8.33 (d, *J* = 8.4 Hz, 1H), 8.21 (d, *J* = 7.5 Hz, 1H), 7.88 (d, *J* = 6.0 Hz, 1H), 7.64 (d, *J* = 3.0 Hz, 1H), 7.48 (d, *J* = 9.1 Hz, 1H), 7.38 (dd, *J* = 9.2, 3.1 Hz, 1H), 6.35 (d, *J* = 6.0 Hz, 1H), 5.28 (s, 2H), 3.82 (s, 9H).

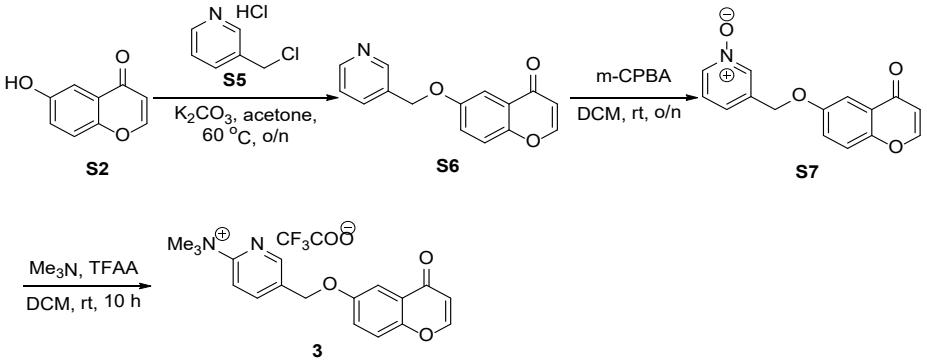


**Scheme 3.** Syntheses of precursor **3**.

*Synthesis of 6-((6-fluoropyridin-3-yl)methoxy)-4H-chromen-4-one (**4**)*

To a solution of 6-hydroxy-4H-chromen-4-one **S2** (50 mg, 0.31 mmol) in acetone (2 mL) was added 5-(chloromethyl)-2-fluoropyridine **3** (45 mg, 0.31 mmol) and $K_2CO_3$ (43 mg, 0.31 mmol) before stirred at 60°C overnight. TLC showed no SM remaining and LCMS showed desired product. The reaction mixture was concentrated and purified by flash (DCM/MeOH = 20/1) to give 6-((6-fluoropyridin-3-yl)methoxy)-4H-chromen-4-one **4** (30.95 mg, 20% for 2 steps) as a pale yellow solid. LCMS (ESI): m/z, 272.08 [M+H]+, RT = 1.882 min. HPLC: 98%, RT = 5.034 min. $^1$H NMR (400 MHz, DMSO-$d_6$) δ 8.39 (s, 1H), 8.29 (d, *J* = 6.0 Hz, 1H), 8.11 (dt, *J* = 8.3, 4.0 Hz, 1H), 7.65 (d, *J* = 9.1 Hz, 1H), 7.55 (d, *J* = 3.1 Hz, 1H), 7.49 (dd, *J* = 9.1, 3.1 Hz, 1H), 7.25 (dd, *J* = 8.5, 2.7 Hz, 1H), 6.34 (d, *J* = 6.0 Hz, 1H), 5.27 (s, 2H).

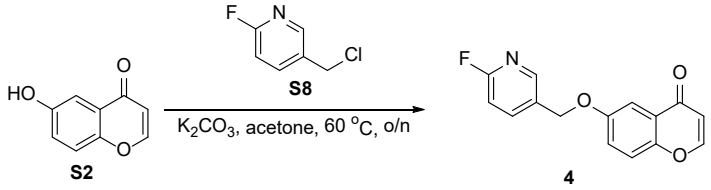


**Scheme 4.** Syntheses of reference standard **4**.

*Synthesis of (6-chloropyridin-3-yl)methan-d2-ol (**S10**)*

To a solution of methyl 6-chloronicotinate **S9** (1 g, 5.83 mmol) was added $LiAlD_4$ (250 mg, 5.83 mmol) in diethyl ether (15 mL) before stirred at -78°C for 2 hours. TLC showed no SM remained. The reaction mixture was diluted white EA and a

small amount of water, dried over $Na_2SO_4$, concentrated to give the (6-chloropyridin-3-yl)methan-d2-ol **S10** (742 mg, 87%) as a red soild.

*Synthesis of 5-(bromomethyl-d2)-2-chloropyridine (**S11**)*

To a solution of (6-chloropyridin-3-yl)methan-d2-ol **S10** (742 mg, 5.10 mmol) in DCM (15 mL) was added $PBr_3$ (1656 mg, 6.12 mmol) dropwise at 0°C before stirred at room temperature for 3 hours. TLC showed no SM remained. The reaction mixture was washed with $NaHCO_3$ (sat) at 0°C and extracted with EA. The organic layer was washed with brine, dried over $Na_2SO_4$ and concentrated to give the 5-(bromomethyl-d2)-2-chloropyridine **3** (755 mg, 71%) as a yellow solid.

*Synthesis of 6-((6-chloropyridin-3-yl)methoxy-d2)-4H-chromen-4-one (**1-D$_2$**)*

To a solution of 6-hydroxy-4H-chromen-4-one **S11** (100 mg, 0.62 mmol) in acetone (3 mL) was added $K_2CO_3$ (63 mg, 0.46 mmol) and stirred at RT for 10 min. To the above mixture was added 5-(bromomethyl-d2)-2-chloropyridine **3** (129 mg, 0.62 mmol) before stirred at 60°C for 3 h. TLC showed 30% SM remained. The reaction mixture was concentrated and purified by Prep-TLC (DCM/MeOH = 20/1) to give 6-((6-chloropyridin-3-yl)methoxy-d2)-4H-chromen-4-one **S12** (120 mg, yield = 63.5%) as a yellow solid. LCMS (ESI): m/z, 290.0 [M+H]+, RT = 1.99 min. HPLC: 100%, RT = 5.06 min. $^1$H NMR (400 MHz, DMSO-$d_6$) δ 8.56 (d, *J* = 2.4 Hz, 1H), 8.30 (dd, *J* = 6.0, 0.8 Hz, 1H), 8.04 - 7.90 (m, 1H), 7.66 (d, *J* = 9.0 Hz, 1H), 7.59 (d, *J* = 8.2 Hz, 1H), 7.54 (d, *J* = 3.1 Hz, 1H), 7.50 (dd, *J* = 9.1, 3.2 Hz, 1H), 6.35 (dd, *J* = 5.9, 0.9 Hz, 1H).

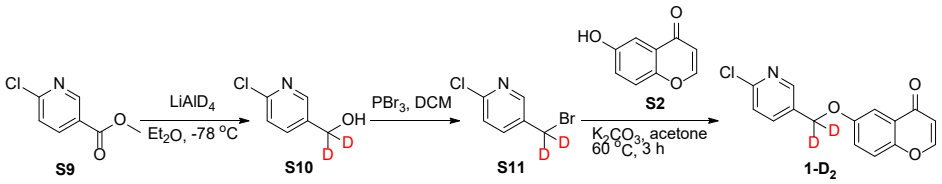


**Scheme 5.** Syntheses of precursor **1-D$_2$**.

*Synthesis of pyridin-3-ylmethan-d2-ol (**S13**)*

To a solution of methyl nicotinate **S12** (5 g, 36.46 mmol) in diethyl ether (30 mL) was added to a suspension of $LiAlD_4$ (1.6 g, 36.46 mmol) in Diethyl ether (20 mL) at -78°C. The mixture was stirred at -78°C for 3 hours. TLC showed no SM remained. The reaction was quenched with water (20 mL) and concentrated in vacuo to move water to give crude desired product which was purified by flash column chromatography (DCM:MeOH = 30:1 to 20:1) on a silica gel to afford the desired product **S13** (3.2 g, 79% yield) as a yellow oil.

*Synthesis of 3-(chloromethyl-d2)pyridine hydrochloride (**S14**)*

To a solution of pyridin-3-ylmethan-d2-ol **S13** (2.1 g, 18.90 mmol) in DCM (20 mL) was added $SOCl_2$ (9 g, 75.58 mmol) dropwise at 0°C. The mixture was stirred at 42°C for 4 hours. TLC showed no SM remained. The reaction mixture was concentrated to give 3-(chloromethyl-d2)pyridine hydrochloride **S14** (2.9 g, 94%) as a white solid.

*Synthesis of 6-(pyridin-3-ylmethoxy-d2)-4H-chromen-4-one (**S15**)*

To a solution of 6-hydroxy-4H-chromen-4-one **S14** (2.4 g, 14.80 mmol) in acetone (50 mL) was added 3-(chloromethyl-d2) pyridine hydrochloride **3** (2.9 g, 17.76 mmol) and $K_2CO_3$ (8.2 g, 59.20 mmol). The mixture was stirred at 60°C overnight. TLC showed no SM remaining and LCMS showed desired product. After cooling to room temperature, the reaction was quenched with water (200 mL) and diluted with ethyl acetate (100 mL). The organic layer was separated, and the aqueous layer was extracted with ethyl acetate (2 × 100 mL). The combined organic layers were washed with water, brine, dried over $Na_2SO_4$, filtered, and concentrated in vacuo. The crude product was purified by flash column chromatography (ethyl acetate/petrol = 1:1 to DCM/MeOH = 30:1) on a silica gel to afford the desired product **S15** (3 g, 79% yield) as a yellow solid.

*Synthesis of 3-(((4-oxo-4H-chromen-6-yl)oxy)methyl-d2)pyridine 1-oxide (**S16**)*

To a solution of 6-(pyridin-3-ylmethoxy-d2)-4H-chromen-4-one **S15** (3 g, 11.75 mmol) in DCM (100 mL) was added m-CPBA (3.8 g, 18.80 mmol). The mixture was stirred at 25°C overnight. TLC showed no SM remaining and LCMS showed desired product. The reaction was quenched with water (200 mL) and diluted with DCM (100 mL). The organic layer was separated, and the aqueous layer was extracted with DCM (2 × 50 mL). The combined organic layers were washed with water, brine, dried over $Na_2SO_4$, filtered, and concentrated in vacuo. The crude product was purified by flash column chromatography (DCM:MeOH = 50:1 to 10:1) on a silica gel to afford the desired product **S16** (3.3 g, 95% yield) as a white solid.

*Synthesis of N,N,N-trimethyl-5-(((4-oxo-4H-chromen-6-yl)oxy)methyl-d2)pyridin-2-aminium 2,2,2-trifluoroacetate (**3-D$_2$**)*

To a solution of 3-(((4-oxo-4H-chromen-6-yl)oxy)methyl-d2)pyridine 1-oxide **S16** (2 g, 7.37 mmol) in DCM (40 mL) was added $Me_3N$ (11 mL, 22.12 mmol, 2 M) and TFAA (4.7 g, 22.12 mmol). The mixture was stirred at 25°C overnight. TLC showed much SM remaining and LCMS showed 10% of the desired product. The reaction was concentrated in vacuo to give crude, which was dissolved in $H_2O$, washed with DCM/MeOH = 10:1 (50 mL) for 10 times. The aqueous phase was freezed dry to give crude desired product. The crude desired product was purified by prep-HPLC (ACN/0.1% TFA in $H_2O$) to afford the desired product **3-D$_2$** (60 mg, 2% yield) as a white solid. LC-MS (+ESI): m/z = 313.2 (M+1), HPLC: 99%, RT = 4.200 min. $^1$H NMR (400 MHz, Chloroform-d) δ 8.64 (d, *J* = 1.8 Hz, 1H), 8.35 (d, *J* = 8.0 Hz, 1H), 8.20 (d, *J* = 7.0 Hz, 1H), 7.87 (d, *J* = 6.0 Hz, 1H), 7.63 (d, *J* = 3.0 Hz, 1H), 7.48 (d, *J* = 9.1 Hz, 1H), 7.37 (dd, *J* = 9.1, 3.1 Hz, 1H), 6.35 (d, *J* = 5.9 Hz, 1H), 3.83 (s, 9H).

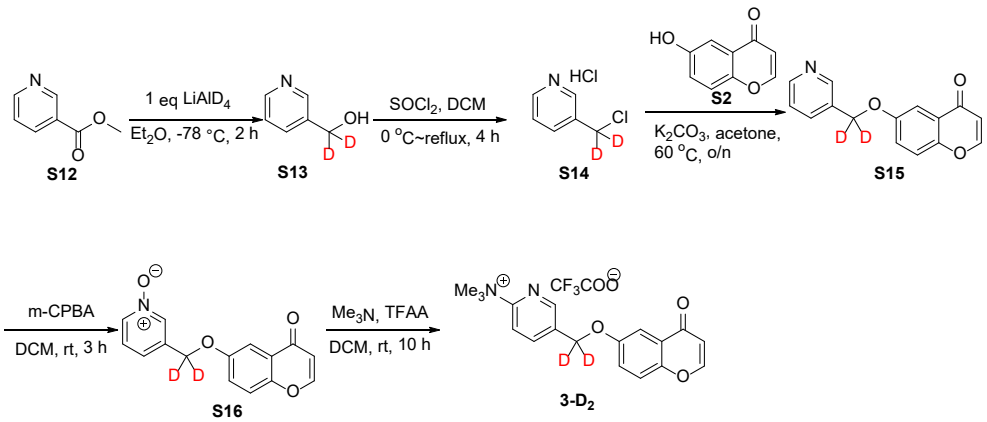


**Scheme 6.** Syntheses of precursor **3-D$_2$**.

*Synthesis of (6-fluoropyridin-3-yl)methan-d2-ol (**S18**)*

To a solution of methyl 6-fluoronicotinate **S17** (100 mg, 0.645 mmol) in diethyl ether (2 mL) was added to a suspension of $LiAlD_4$ (27 mg, 0.645 mmol) in diethyl ether (3 mL) at -78°C. The mixture was stirred at -78°C for 2 hours. TLC showed no SM remained. The reaction mixture was diluted white EA and a small amount of water, dried over $Na_2SO_4$ and concentrated to give the (6-fluoropyridin-3-yl)methan-d2-ol **S18** (82 mg, 99%) as yellow oil.

*Synthesis of 5-(bromomethyl-d2)-2-fluoropyridine (**S19**)*

To a solution of (6-fluoropyridin-3-yl)methan-d2-ol **S18** (82 mg, 0.636 mmol) in DCM (2 mL) was added $PBr_3$ (206 mg, 0.763 mmol) dropwise at 0°C. The mixture was stirred at room temperature for 2 hours. TLC showed no SM remained. The reaction mixture was washed white $NaHCO_3$ (sat) at 0°C and extracted with EA. The organic layer was washed with brine, dried over $Na_2SO_4$ and concentrated to give the 5-(bromomethyl-d2)-2-fluoropyridine **S19** (81 mg, 66%) as yellow oil.

*Synthesis of 6-((6-fluoropyridin-3-yl)methoxy-d2)-4H-chromen-4-one (**4-D$_2$**)*

To a solution of 6-hydroxy-4H-chromen-4-one **S19** (50 mg, 0.31 mmol) in acetone (3 mL) was added $K_2CO_3$ (63 mg, 0.46 mmol) and stirred at RT for 5 min and then added 5-(bromomethyl-d2)-2-fluoropyridine **3** (70 mg, 0.36 mmol) before stirred at 60°C for 3 h. The reaction mixture was concentrated and purified by prep-TLC (DCM/MeOH = 20/1) to give the 6-((6-fluoropyridin-3-yl)methoxy-d2)-4H-chromen-4-one **4-D$_2$** (65 mg, yield = 70%) as a yellow solid. LCMS (ESI): m/z, 274.15 [M+H]+, RT = 1.92 min. HPLC: 98%, RT = 4.11 min. $^1$H NMR (400 MHz, DMSO-$d_6$) δ 8.39 (d, *J* = 2.4 Hz, 1H), 8.29 (d, *J* = 6.0 Hz, 1H), 8.12 (td, *J* = 8.2, 2.5 Hz, 1H), 7.65 (d, *J* = 9.1 Hz, 1H), 7.55 (d, *J* = 3.1 Hz, 1H), 7.49 (dd, *J* = 9.1, 3.2 Hz, 1H), 7.25 (dd, *J* = 8.4, 2.7 Hz, 1H), 6.34 (d, *J* = 6.0 Hz, 1H).

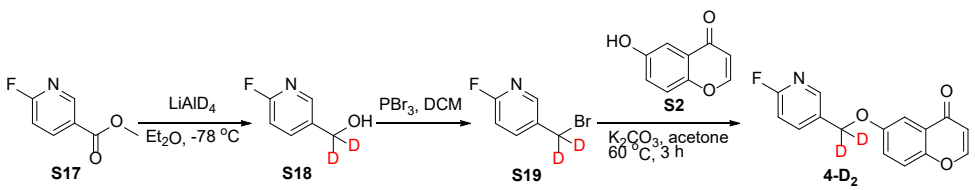


**Scheme 7.** Syntheses of reference standard **4-D$_2$**.

**Table S1.** Radiochemical Synthesis of [$^{18}$F]**4** and Radiochemical parameter exploration of precursor **1**

| Precursor (mg) | Base (mg) | Solvent (μL) | Reaction time (min) | Reaction temperature (°C) | Radiochemical purity (%) | n.d.c RCY (%) |
|---|---|---|---|---|---|---|
| 2 | $K_2CO_3$(2) + $K_{2.2.2}$(10) | DMSO(600) | 10 | 125 | 30 | 1.1 |
| 2 | $K_2CO_3$(4) + $K_{2.2.2}$(20) | DMSO(600) | 10 | 125 | 15 | 0.3 |
| 2 | $K_2CO_3$(1) + $K_{2.2.2}$(5) | DMSO(600) | 10 | 125 | 35 | 1.6 |
| 2 | $K_2CO_3$(0.5) + $K_{2.2.2}$(5) | DMSO(600) | 10 | 125 | 41 | 0.9 |
| 2 | $K_2CO_3$(2) + $K_{2.2.2}$(10) | DMF(600) | 10 | 125 | 27 | 1.1 |
| 2 | $K_2CO_3$(4) + $K_{2.2.2}$(20) | DMF(600) | 10 | 125 | 30 | 0.6 |
| 2 | $K_2CO_3$(1) + $K_{2.2.2}$(5) | DMF(600) | 10 | 125 | 14 | 0.4 |
| 2 | $K_2CO_3$(0.5) + $K_{2.2.2}$(5) | DMF(600) | 10 | 125 | 28 | 0.2 |
| 2 | TBAB(2) | DMF(600) | 10 | 125 | 4 | 0.5 |
| 2 | TBAB(4) | DMF(600) | 10 | 125 | 15 | 0.3 |
| 2 | TBAB(2) | DMF(600) | 10 | 150 | 57 | 1.0 |
| 2 | TBAB(2) | DMF(600) | 10 | 180 | 70 | 3.9 |

**Table S2.** Radiochemical Synthesis of [$^{18}$F]**4** and Radiochemical parameter exploration of precursor **2**

| Precursor (mg) | Base (mg) | Solvent (μL) | Reaction time (min) | Reaction temperature (°C) | Radiochemical purity (%) | n.d.c RCY (%) |
|---|---|---|---|---|---|---|
| 2 | $K_2CO_3$(2) + $K_{2.2.2}$(10) | DMSO(600) | 10 | 125 | <1 | <0.1 |
| 2 | $K_2CO_3$(4) + $K_{2.2.2}$(20) | DMSO(600) | 10 | 125 | <1 | <0.1 |
| 2 | TEAB(2) | DMSO(600) | 10 | 125 | <1 | <0.1 |
| 2 | TEAB(1) | DMSO(600) | 10 | 125 | <1 | <0.1 |
| 2 | TEAB(0.5) | DMSO(600) | 10 | 125 | <1 | <0.1 |
| 2 | TBAB(2) | DMSO(600) | 10 | 125 | <1 | <0.1 |
| 2 | $K_2CO_3$(1) + $K_{2.2.2}$(5) | DMSO(600) | 10 | 100 | <1 | <0.1 |
| 2 | $K_2CO_3$(1) + $K_{2.2.2}$(5) | DMSO(600) | 10 | 80 | <1 | <0.1 |
| 2 | $K_2CO_3$(1) + $K_{2.2.2}$(5) | ACN(600) | 10 | 60 | <1 | <0.1 |

**Table S3.** Radiochemical parameter and In vitro characterization of [$^{18}$F]**4**

| Entry | n.d.c RCY (%) | MA (Ci/μmol) | LogD (pH 7.4) | LogP | tPSA |
|---|---|---|---|---|---|
| [$^{18}$F]**4** | 11±1 | 8.3±1.3 | 2.36 | 2.27 | 47.89 |

**Table S4.** Radiochemical parameter and In vitro characterization of [$^{18}$F]**4-D$_2$**

| Entry | n.d.c RCY (%) | MA (Ci/μmol) | LogD (pH 7.4) | LogP | tPSA |
|---|---|---|---|---|---|
| [$^{18}$F]**4-D$_2$** | 12±1 | 8.1±2.4 | 2.35 | 2.27 | 47.89 |

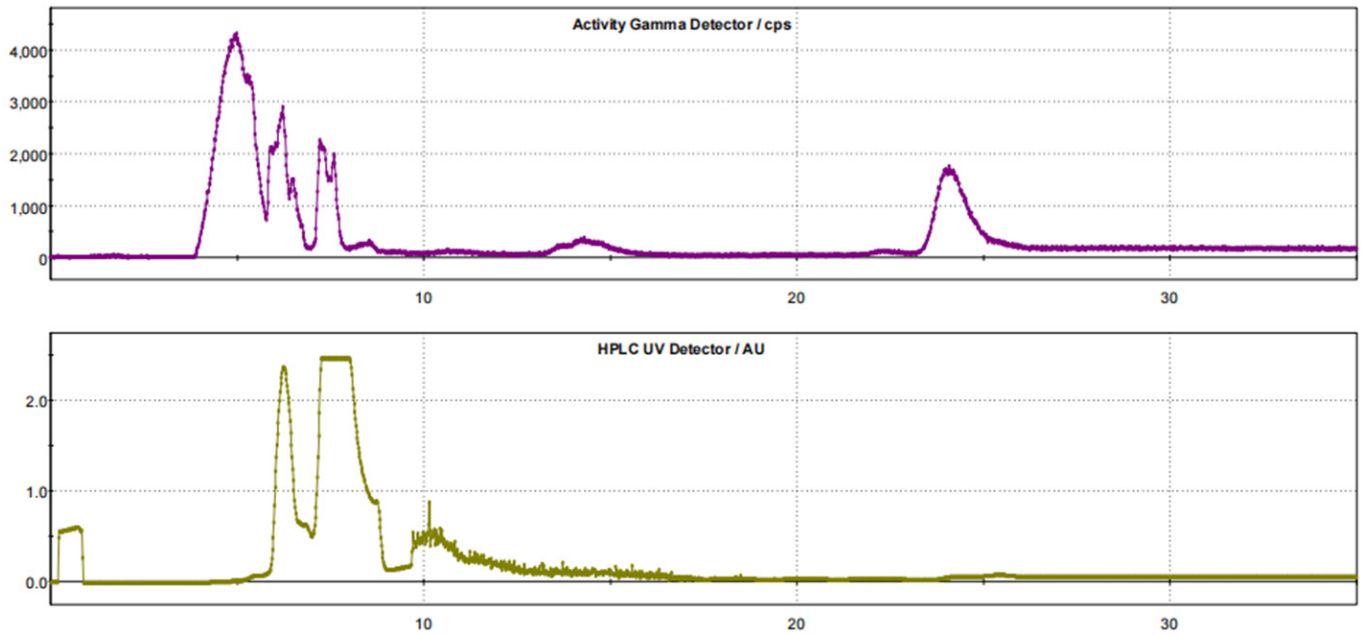


**Figure S1.** HPLC chromatogram of the semipreparative purification of [$^{18}$F]**4**.

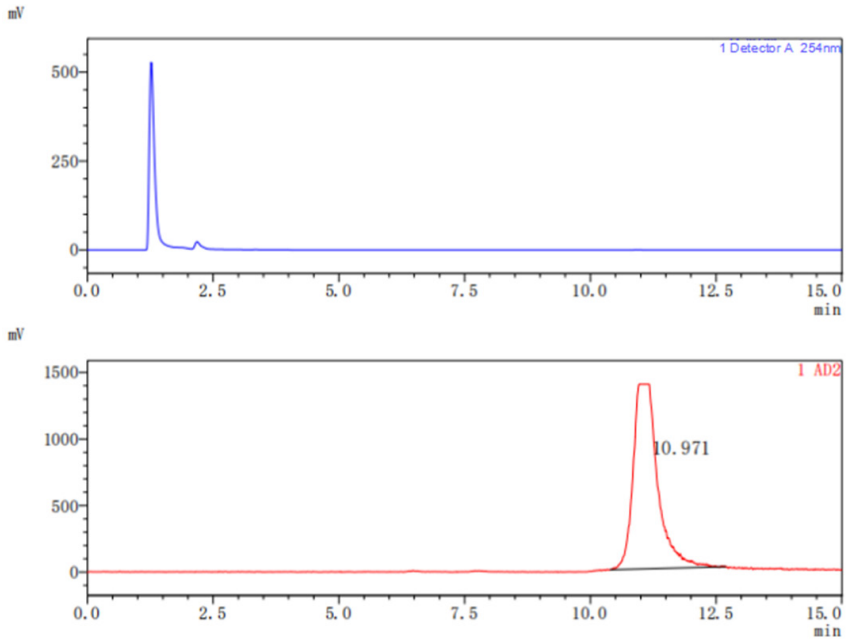


**Figure S2.** HPLC chromatogram of the analysis of [$^{18}$F]**4** co-injected with the cold reference standard.

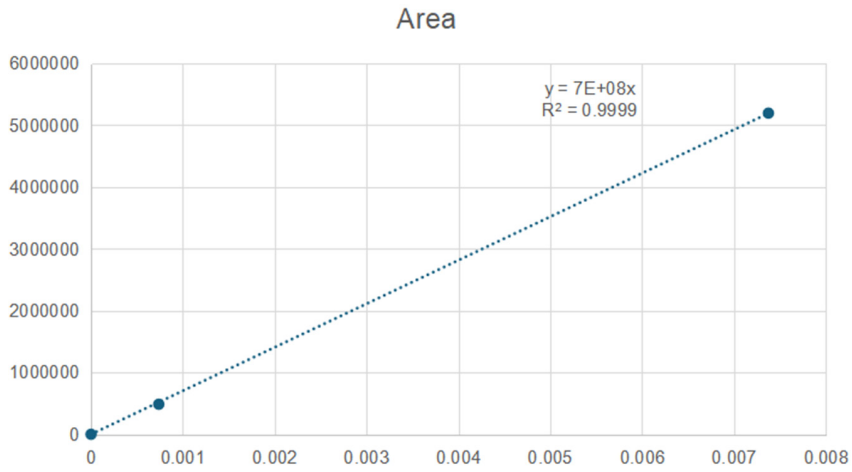


**Figure S3.** Standard curve of [$^{18}$F]**4**.

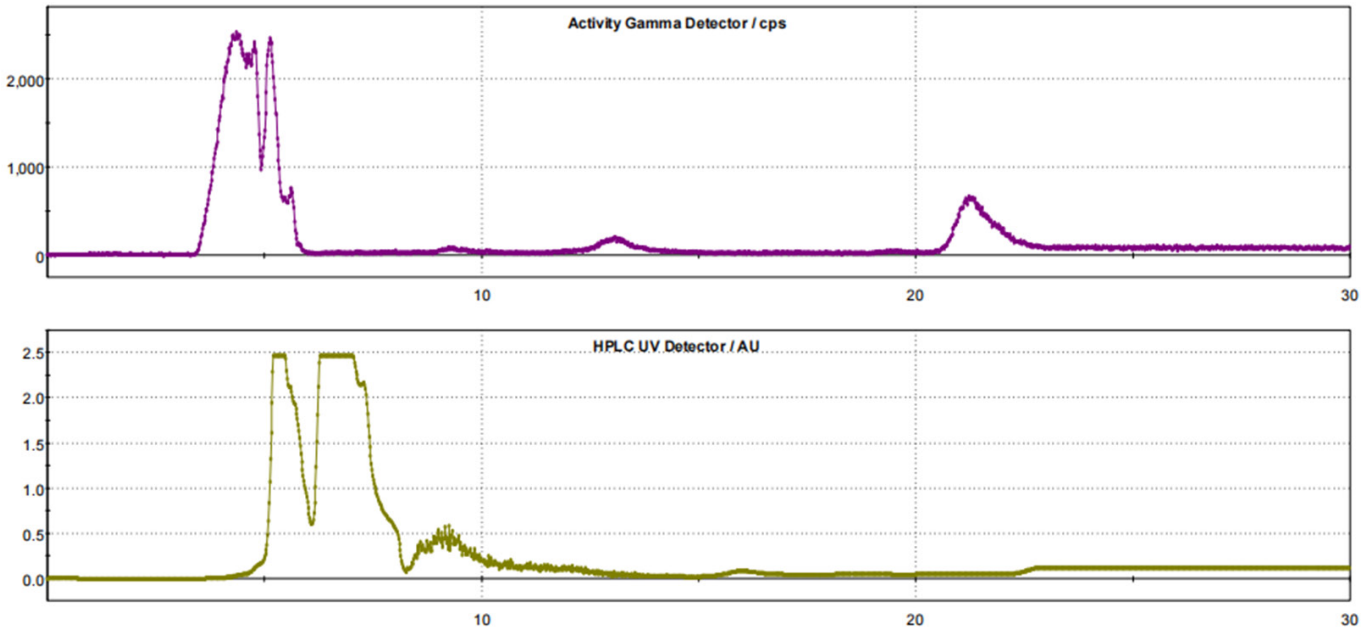


**Figure S4.** HPLC chromatogram of the semipreparative purification of [$^{18}$F]**4-D$_2$**.

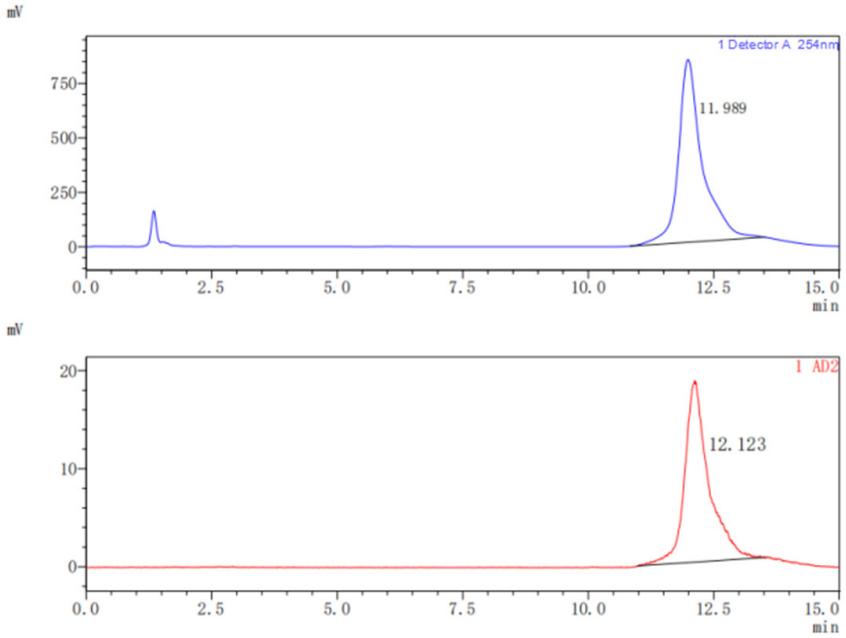


**Figure S5.** HPLC chromatogram of the analysis of [$^{18}$F]**4-D$_2$** co-injected with the cold reference standard.

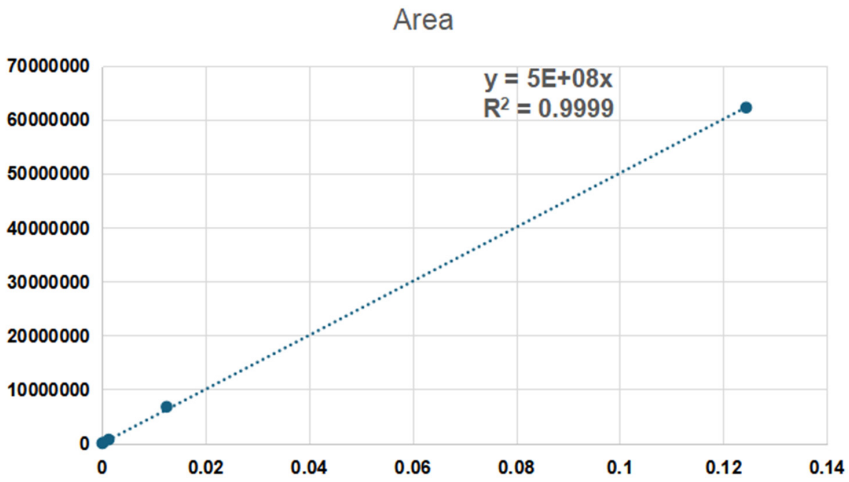


**Figure S6.** Standard curve of [$^{18}$F]**4-D$_2$**.

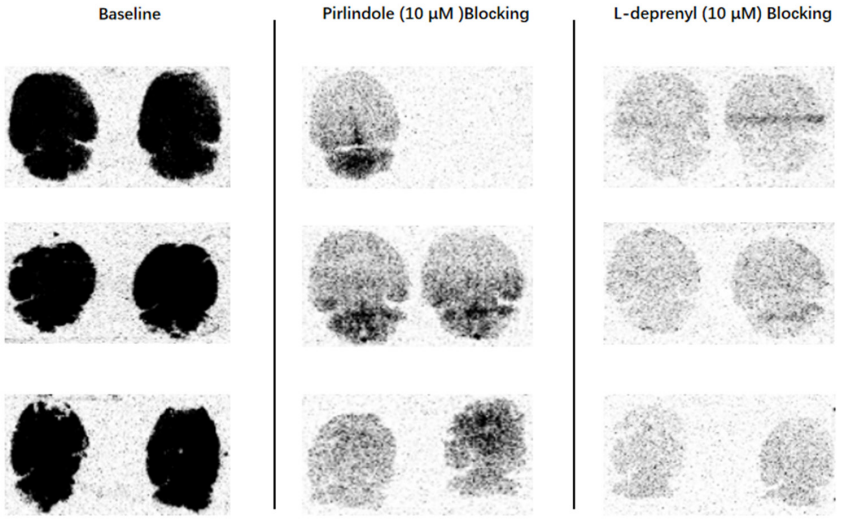


**Figure S7.** In vitro autoradiography of [$^{18}$F]**4-D$_2$** on rat brain cross sections. Baseline: n = 6; Pirlindole: n = 5; L-deprenyl: n = 6.


**Figure S8.** $^1$H NMR spectrum of **S2**.

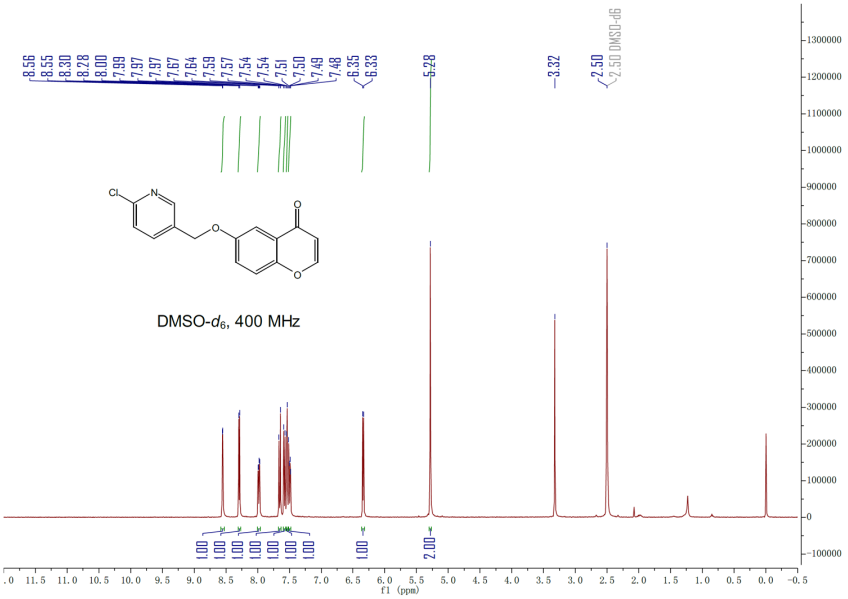


**Figure S9.** $^1$H NMR spectrum of **1**.

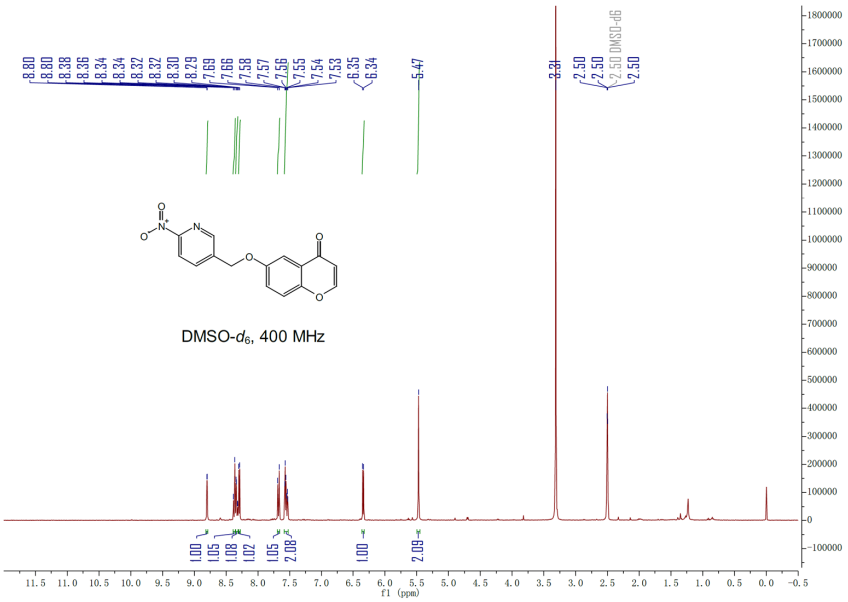


**Figure S10.** $^1$H NMR spectrum of **2**.

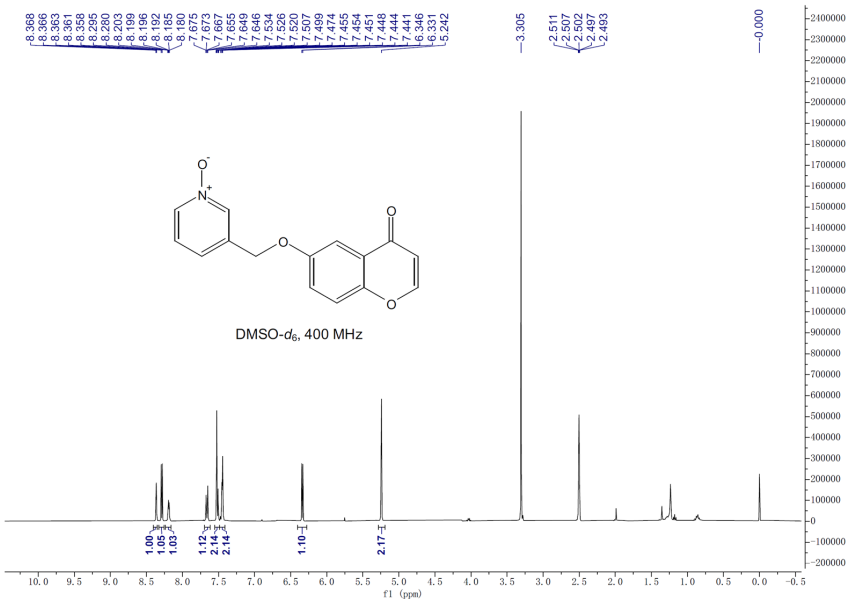


**Figure S11.** $^1$H NMR spectrum of **S7**.

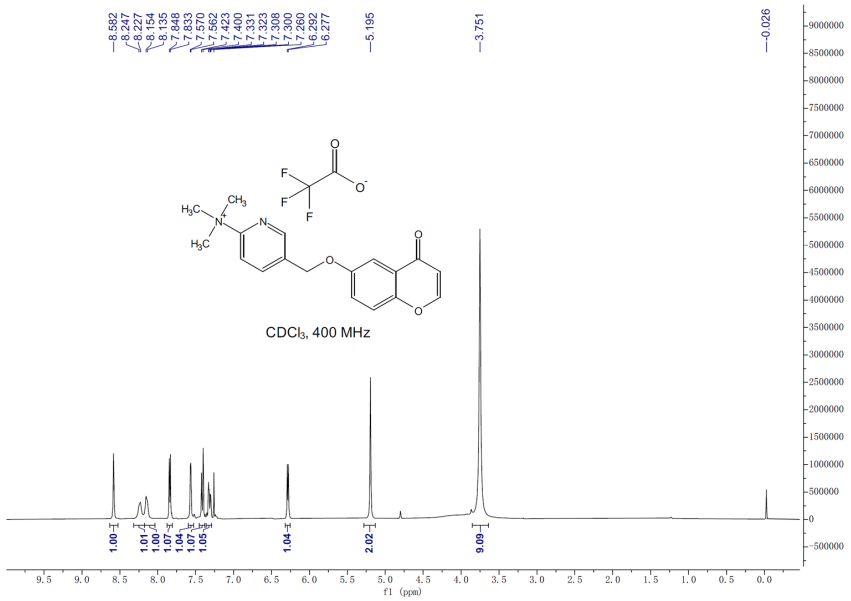


**Figure S12.** $^1$H NMR spectrum of **3**.

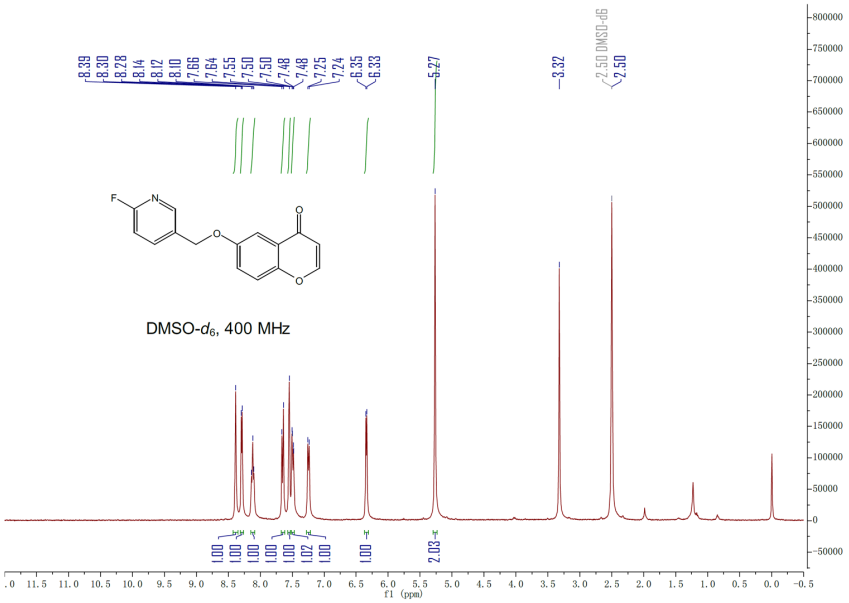


**Figure S13.** $^1$H NMR spectrum of **4**.

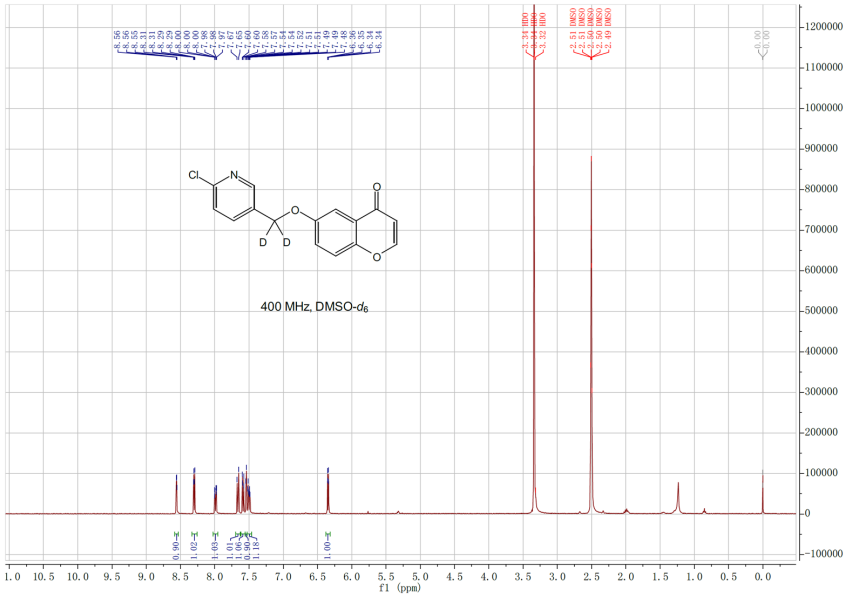


**Figure S14.** $^1$H NMR spectrum of **1-D$_2$**.

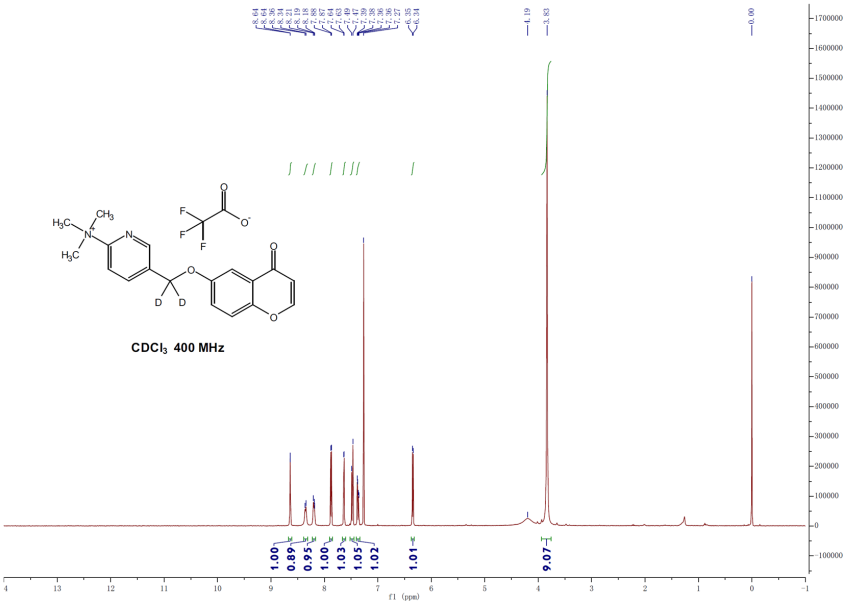


**Figure S15.** $^{1}$H NMR spectrum of **3-D$_2$**.

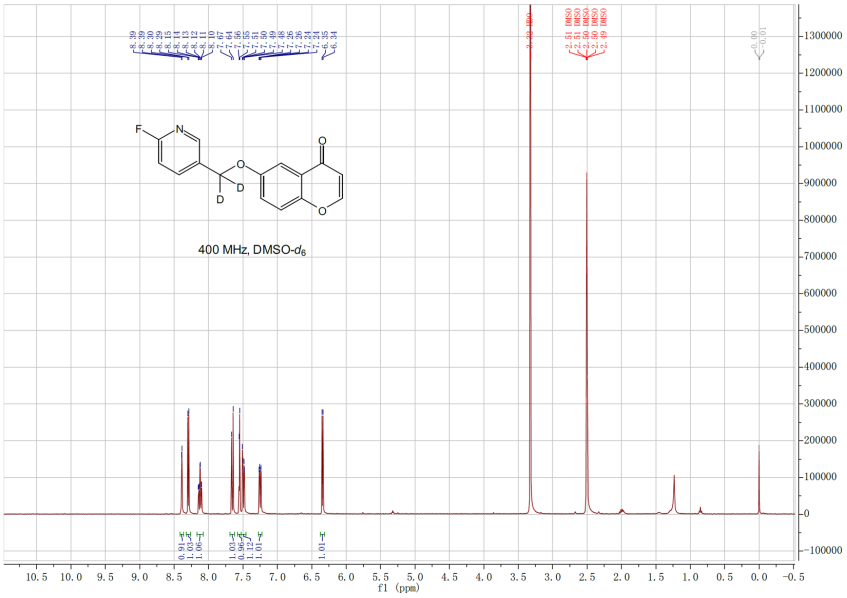


**Figure S16.** $^{1}$H NMR spectrum of **4-D$_2$**.

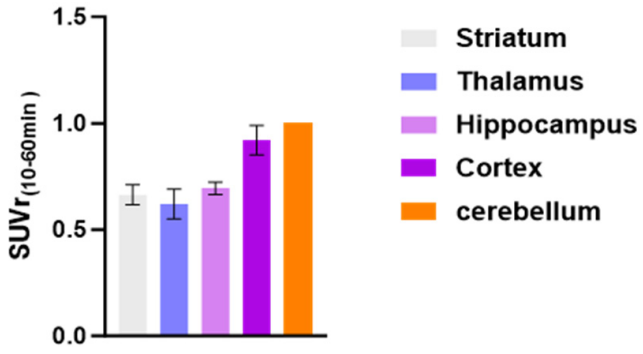


**Figure S17.** Quantitative analysis of the standardized uptake value ratios (SUVrs) for [$^{18}$F]**4** across various brain regions in rats under baseline conditions, with the cerebellum serving as the reference region.

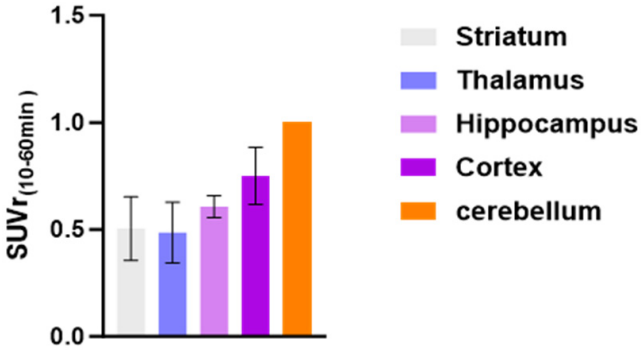


**Figure S18.** Quantitative analysis of the SUVrs for [$^{18}$F]**4-D$_2$** across various brain regions in rats under baseline conditions, with the cerebellum serving as the reference region.

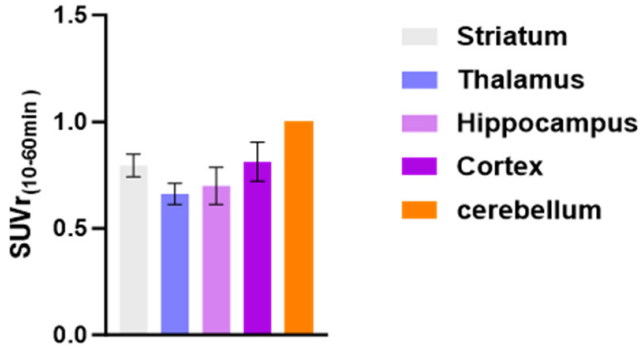


**Figure S19.** Quantitative analysis of the standardized uptake value ratios (SUVrs) for [$^{18}$F]**4-D$_2$** across various brain regions in mice under baseline conditions, with the cerebellum serving as the reference region.

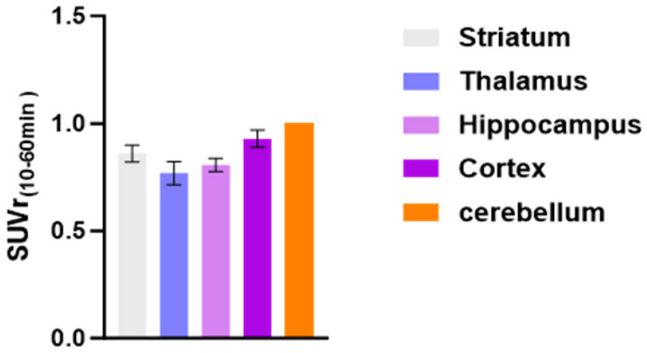


**Figure S20.** Quantitative analysis of the standardized uptake value ratios (SUVrs) for [$^{18}$F]**4-D$_2$** across various brain regions in mice under pre-blocking conditions, with the cerebellum serving as the reference region.

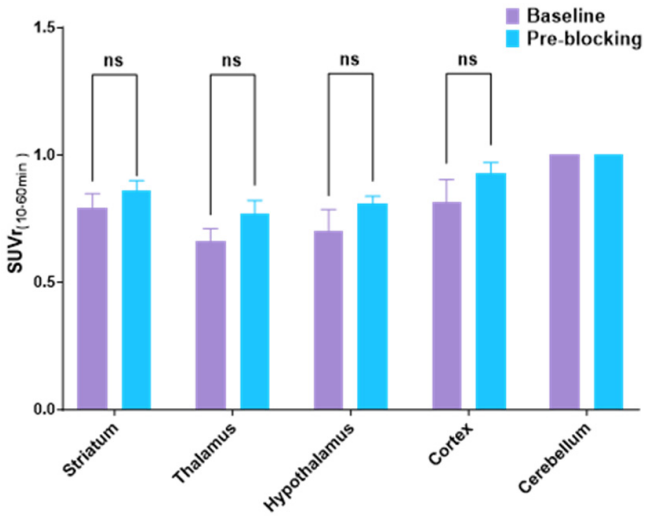


**Figure S21.** Comparative analysis of the SUVRs for[$^{18}$F]**4-D$_2$** across different brain regions in mice under both baseline and pre-blocking conditions, with the cerebellum serving as the reference region (n = 3).